Initiation of solution NMR studies on the bacterial cell division regulator MinD

Adam Cloutier

Thesis submitted in partial fulfillment
of the requirements for the degree
of Masters of Science in Chemistry

© Adam Cloutier, Ottawa, Canada, 2019

Abstract

Bacterial cell division relies on the cell division septum to form at the mid-cell position. In gram negative bacteria, this is mediated by three proteins, MinC, MinD and MinE. Together these proteins interact with each other and the membrane in a dynamic, oscillating process which prevents cell division septum formation at the cell poles. The early phase of this process involves MinD binding to the membrane, which is triggered upon binding of ATP. Subsequent interactions with MinE result in stimulation of the ATPase activity of MinD. After hydrolysis, MinD is released from the membrane and diffuses to a new binding site. Many *in* silico models have been constructed of the Min system in an attempt to describe its self-organizing behaviour. A limitation of these models is that, in order to prevent rapid re-binding of MinD to the membrane after hydrolysis of ATP, the exchange of bound ADP for ATP is assumed to be a slow process, on the order of $1s^{-1}$. In order to provide experimental evidence of the rate of nucleotide binding, we performed a series of triple-resonance NMR experiments to complete a partial assignment of backbone atom resonances, which required the application of deuterium labelling and amino acid-specific selective unlabelling. After the introduction of ATP, it was discovered that no dimerization had been induced, in contrast with existing literature. It was proposed that MinD from *N. gonorrhoeae* only forms a dimer in the presence of a membrane, while literature with MinD from *E. coli* shows it does not have this requirement. Interestingly while dimerization had not been induced, there was a persistent population of dimeric species even in the absence of nucleotide. This was discovered to be the result of disulfide formation, likely an artifact of established purification protocols. Binding of both ADP and ATP to MinD were studied by titration using NMR, with the relative affinity of both nucleotides to MinD being indistinguishable. By analyzing peak coalescence in the half-bound condition, a maximum rate was determined for nucleotide binding, with the lifetime being on the order of 170ms. Results from this experiment support models requiring a slow nucleotide binding step, and help enhance understanding of how Min proteins sustain oscillations required for normal cell division.

Acknowledgements

To Dr. Natalie K. Goto, thank you for your endless patience. You opened your doors for an inexperienced undergraduate and have nurtured me through this whole process. You have always held me to a high standard, to which I owe my success. I am most thankful for the trust and confidence you placed in me. In the moments I didn't think it would work out, you were always there to guide me through it. I hope to go forward with the same curiosity you have inspired in me.

To Dr. Glenn Facey and Dr. Peter Pallister, I would like to extend my thanks for all the help provided in not only the running of the NMR spectrometers, but especially the preparation and execution of deuterium-decoupled pulse programs. I appreciate the patience with which you approached my somewhat unique problems, many of which I'm certain were my own doing.

To Dr. Yves Aubin and the NMR facility at Health Canada, thank you for your assistance in carrying out triple-resonance experiments. I am grateful for the time you volunteered on your NMR spectrometer, and your assistance in getting our spectrometer to perform to the same level.

To Dr. Roberto Chica and Dr. Jeff Keillor, I am grateful for allowing me to access your labs and use your instruments. Many of these experiments wouldn't have been possible without your support.

To Saud Ayed and Alex Foo, I am glad to have been able to spend time working with you and learning all about lab life. I owe all my success in the lab to your teaching, and appreciate your tolerance of my very frequent questions.

To Krishna Gelda, Kristopher Fequet, Liam Charron, Minh Hieu Tran, and Medhani Mohottalage, thank you for all your assistance in the lab. While my goal was to impart as much knowledge as I could, your assistance with experiments, data analysis, and just being there for me to bounce ideas off was invaluable.

To Anwar Hassan, I've enjoyed troubleshooting the multitude of challenges your project presents, and am glad you tolerated my endless ranting about whatever was on my mind that day.

To Adam Damry and Matt Eason, you were always there when I needed you. If a machine stopped working, if my data made no sense, and even if I goofed and was trying to save a sample, you always had time to think through the problem with me and offer a solution. I couldn't have succeeded without all your wisdom.

And of course to my family, who through seemingly endless years of school have made sure I was ready for success. While I know the contents of this thesis might be a bit too specialized, I appreciate that you take an interest in my work and have learned all about my project. Thank you for all your support throughout my school years.

Contents

List of Figures

List of Abbreviations

ADP	Adenosine diphosphate
ATP	Adenosine triphosphate
CD	Circular dichroism
EDTA	Ethylenediaminetetraacetic acid
FPLC	Fast protein liquid chromatography
GFP	Green fluorescent protein
HSQC	Heteronuclear single quantum coherence
IPTG	Isopropyl β-D-1-thiogalactopyranoside
K_D	Dissociation constant
MALS	Multi angle light scattering
MinD_{Ec}	MinD encoded by *E. coli*
MinD_{Ng}	MinD encoded by *N. gonorrhoeae*
MTS	Membrane targeting sequence
NMR	Nuclear magnetic resonance
OD	Optical density
PDB	Protein Databank
RI	Refractive index
T_1	Longitudinal relaxation
T_2	Transverse relaxation
TCEP	Tris(2-carboxyethyl)phosphine
TIRF	Total internal refraction fluorescence
TROSY	Transverse relaxation optimized spectroscopy

1 Introduction

1.1 Role of the Min system in symmetric bacterial cell division

Bacterial cell division relies on the duplication of DNA and the ability to segregate this, and other intracellular components, into two identical daughter cells. This is achieved by the formation of the cell division septum at the mid-cell position, producing two daughter cells of equal size. Failure to properly localize the septum results in the formation of irregularly-sized daughter cells. In rod-shaped cells like E. coli, this gives rise to cells with elongated, filamentous morphology or small, anucleate cells that lack DNA and are incapable of further rounds of cell division (1). These phenotypes are the result of unrestricted placement of the cell division septum, allowing division to occur near the cell pole (2), a phenotype that can arise from mutations in the *minB* operon (3–6).

In gram negative bacteria, division septum localization is controlled by two complementary systems: nucleoid occlusion, preventing septum formation at the nucleoid; and the Min system, comprised of three proteins encoded by the *minB* operon: MinC, MinD, and MinE (5). Together these three Min proteins inhibit polymerization of FtsZ into the Z-ring in a site-specific manner, allowing Z ring formation at the mid-cell position but not at the cell poles (7). Only MinC directly inhibits FtsZ assembly, while MinD and MinE serve to control localization of MinC, restricting it to zones near the cell poles. This serves to concentrate MinC near the cell poles and away from the mid-cell, allowing FtsZ assembly only at the mid-cell position.

The critical role the Min system plays in bacterial cell division makes it an enticing target for the development of new antibiotics, particularly given the increasing prevalence of antibiotic-resistant pathogens, the result of decades of over-use (8). One such example is *Neisseria gonorrhoeae*, which is responsible for the sexually transmitted disease gonorrhoea. In recent years, multi-drug resistant strains of *N. gonorrhoeae* have been identified in patients, raising concerns about our continuing ability to treat infections and emphasizing the need for development of new antibiotics (9–11). The Min system, lacking any human homologue, is of special interest for the development of new antibiotics: when the Min system in *N. gonorrhoeae* is disrupted, the cells undergo lysis (12), and cell adherence and virulence are reduced (13, 14).

While in this thesis I focus on MinD from *N. gonorrhoeae*, the majority of the knowledge about the functionality of the Min system arises from studies on the *E. coli* homologues (15). MinD from *E. coli* and *N. gonorrhoeae* are highly homologous, with 75% sequence identity (Figure 1.1) and lower levels of sequence conservation constrained to regions predicted to be in unstructured loops, suggesting that the *N. gonnorrhoeae* MinD ($MinD_{Ng}$) should adopt the same structure as the E. coli homologue ($MinD_{Ec}$). This is also supported by studies of *ΔminB E. coli* cells transformed with vectors expressing $MinD_{Ng}$ and either $MinE_{Ng}$ or $MinE_{Ec}$: in both situations normal Min protein localization was observed, demonstrating that the MinD-MinE interaction is conserved across species. (16, 17)

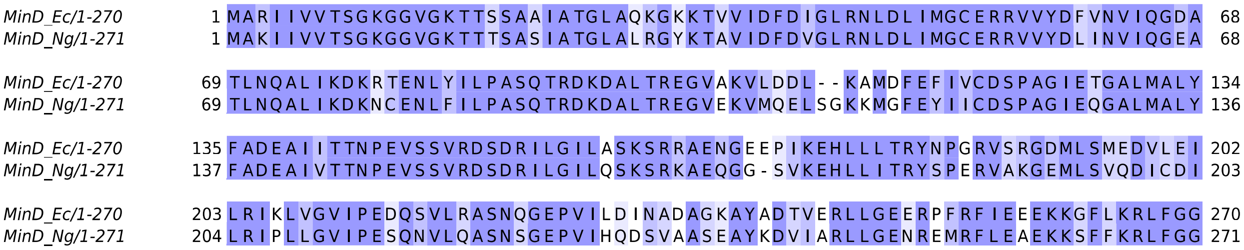

```
MinD_Ec/1-270     1 MARIIVVTSGKGGVGKTTSSAAIATGLAQKGKKTVVIDFDIGLRNLDLIMGCERRVVYDFVNVIQGDA  68
MinD_Ng/1-271     1 MAKIIVVTSGKGGVGKTTTSASIATGLALRGYKTAVIDFDVGLRNLDLIMGCERRVVYDLINVIQGEA  68

MinD_Ec/1-270    69 TLNQALIKDKRTENLYILPASQTRDKDALTREGVAKVLDDL--KAMDFEFIVCDSPAGIETGALMALY 134
MinD_Ng/1-271    69 TLNQALIKDKNCENLFILPASQTRDKDALTREGVEKVMQELSGKKMGFEYIICDSPAGIEQGALMALY 136

MinD_Ec/1-270   135 FADEAIITTNPEVSSVRDSDRILGILASKSRRAENGEEPIKEHLLLTRYNPGRVSRGDMLSMEDVLEI 202
MinD_Ng/1-271   137 FADEAIVTTNPEVSSVRDSDRILGILQSKSRKAEQGG-SVKEHLLITRYSPERVAKGEMLSVQDICDI 203

MinD_Ec/1-270   203 LRIKLVGVIPEDQSVLRASNQGEPVILDINADAGKAYADTVERLLGEERPFRFIEEEKKGFLKRLFGG 270
MinD_Ng/1-271   204 LRIPLLGVIPESQNVLQASNSGEPVIHQDSVAASEAYKDVIARLLGENREMRFLEAEKKSFFKRLFGG 271
```

Figure 1.1 Amino acid sequence alignment of $MinD_{Ec}$ and $MinD_{Ng}$. Sequences were obtained from Uniprot and aligned using Clustal Omega (90, 91). Sequences were colored by BLOSUM62 score using Jalview (92, 93).

This localization by the Min proteins is not a static process, and gives rise to a time-averaged concentration gradient in a process outlined in Figure 1.2. As shown by microscopy of fluorescently-tagged Min proteins, MinD associates with the membrane to form a concentrated zone at one cell pole, with MinC colocalizing with this region (18). In this zone MinD appears to polymerize on the membrane, forming a coiled superstructure that electron microscopy of isolated MinD on membranes suggest is made of filaments of MinD polymer (19, 20). MinE accumulates in a smaller concentrated zone at the edge of the MinCD-rich region, called the E-ring (21). In a process that typically takes less than a minute, the MinCD zone shrinks towards the pole, followed by the E-ring until the MinCD region disappears entirely (22, 23). A new MinCD region begins to form at the other cell pole while the E-ring dissipates. When the MinCD region almost reaches the mid-point of the cell, another E-ring assembles at the edge of the MinCD region, causing it to shrink with the E-ring following the trailing edge until it disappears, and the cycle begins again (24, 25). The result of this coordinated pole-to-pole oscillation of Min proteins gives rise to a concentration of the MinCD complex that is lowest in the mid-cell region.

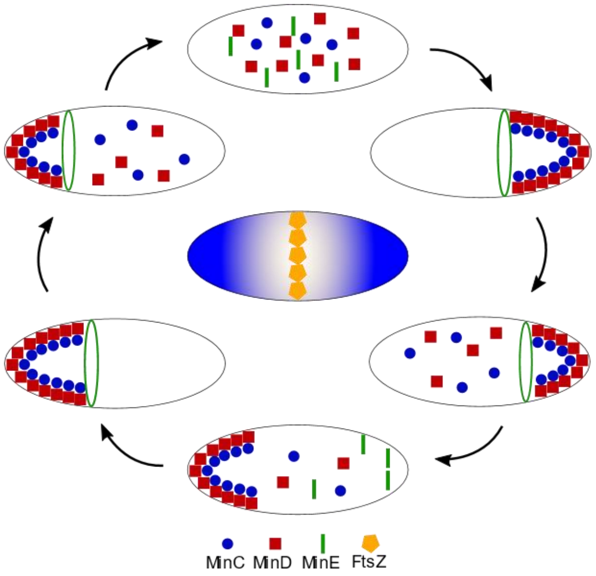

Figure 1.2. Schematic overview of Min protein oscillation inside bacterial cells. Clockwise, from top: Min proteins in the cytoplasm; MinD chaperones MinC to a cell pole, while MinE forms a ring near the edge of this region; the E-ring moves towards the cell pole, displacing MinC and MinD; MinC and MinD localize to the membrane at the opposing cell pole; MinE forms a ring near the edge of this new region; and MinE moves towards this cell pole, displacing MinC and MinD. Center: the time-averaged concentration gradient of MinC is drawn, with FtsZ polymerization depicted at the mid-cell.

The molecular mechanism behind this oscillating behaviour has been explored through a number of biochemical studies and is illustrated in Figure 1.3. This process begins with the binding of MinD and ATP which through size exclusion chromatography has been shown to induce dimerization, while ADP-bound MinD is monomeric (26–28). The binding of ATP also causes MinD to localize to the membrane as reported from sedimentation assays (22, 27, 29, 30). These assays have also revealed that once membrane-bound, MinD is able to bind MinC to form the MinCD complex, termed the inhibitory complex due to its ability to inhibit FtsZ polymerization (23, 31–33).

In the absence of MinD and ATP, fluorescence microscopy shows that MinE localizes to the cytoplasm (21). According to lipid vesicle sedimentation studies, MinE can bind the lipid membrane, but only in the presence of ATP-bound MinD (31). Yeast three-hybrid experiments have demonstrated that MinE can disrupt the MinCD complex, suggesting that MinE and MinC compete for overlapping binding sites on MinD (33, 34). The MinE-MinD interaction has been shown to be of higher affinity than the MinC-MinD interaction, with sedimentation assays showing MinE was able to displace MinC from membrane-bound MinD, while MinC was unable to do so to MinE (28). Binding of MinE to MinD stimulates the ATPase activity of MinD, increasing hydrolysis rates 10-fold (20, 35, 36). Sedimentation assays have also shown that MinE promotes dissociation of MinD from the membrane, generating the ADP-bound monomeric form of MinD (31). The monomeric form must exchange its bound nucleotide before participating in the cycle again (23, 27).

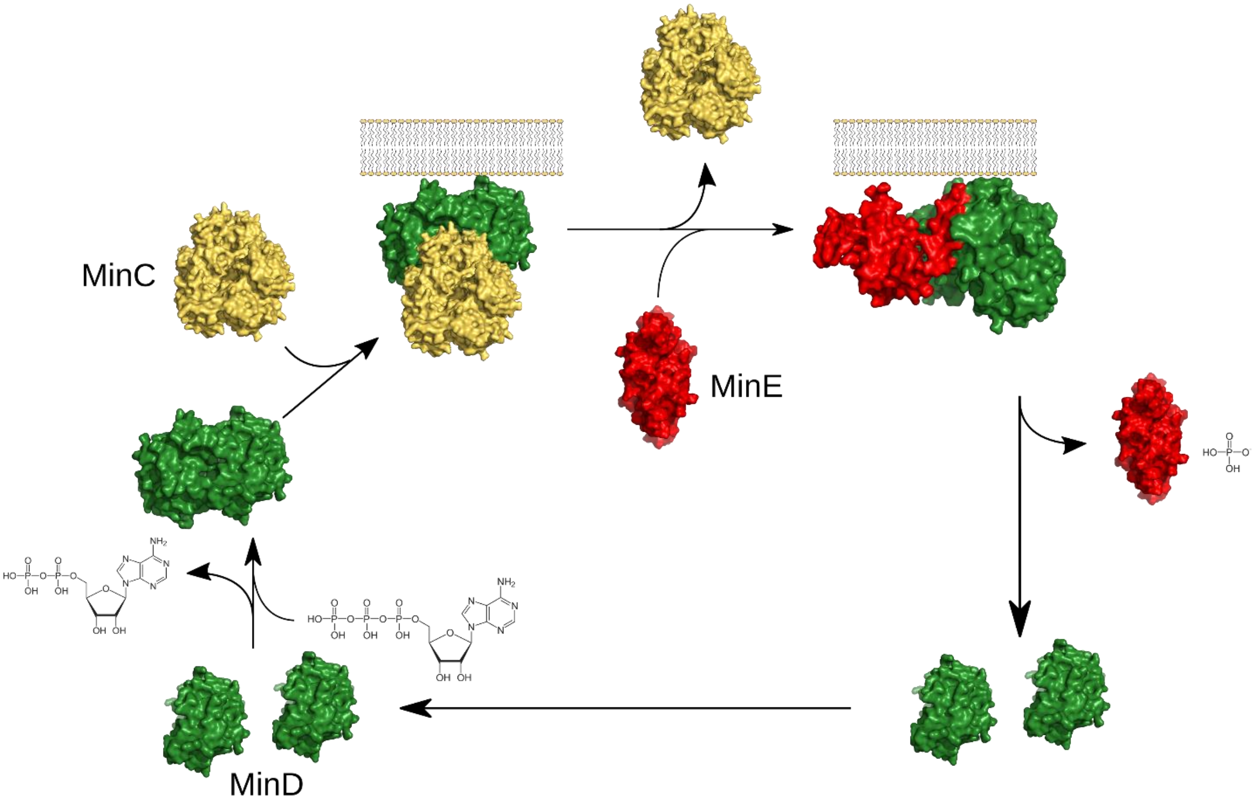

Figure 1.3 The Min protein interaction cycle. Starting from bottom left, clockwise: MinD exchanges bound ADP for ATP and forms a homodimer; MinC is recruited and the MinCD complex binds the membrane; MinE displaces MinC and binds to MinD; MinE-MinD interactions stimulate MinD ATP hydrolysis which leads to dissociation of the complex.

MinD interactions with the membrane have been shown to be mediated by a 10-residue C-terminal region termed the Membrane Targeting Sequence (MTS). In truncations lacking this region MinD fails to localize to the membrane (37). When represented as a helical wheel as in Figure 1.4, charged residues align on one side of the helix, while hydrophobic residues align on the opposing face. Circular dichroism (CD) experiments on a peptide derived from the C-terminus of MinD indicate that this region goes from random coil to a helix structure in the presence of a lipid bilayer (30). Indeed the hydrophobic residues have been shown to be inserted into the lipid bilayer by monitoring tryptophan fluorescence (38). As membrane localization is only seen in the presence of ATP it is suggested that ATP binding, or the dimerization induced by ATP binding, affects the conformation of the MTS and acts as a trigger for membrane binding (29).

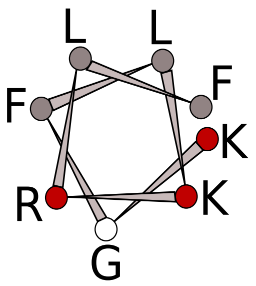

Figure 1.4 Helical wheel representation of the residues comprising the MinD membrane targeting sequence. Hydrophobic residues are depicted as grey, charged are red.

1.2 Structure of MinD

The availability of high-resolution crystal structures of MinD_{Ec} allows greater insight into the mechanism of its oscillation. The structure of the ATP-bound, hydrolysis-deficient MinD_{Ec} D40A ΔC10 revealed that its Walker A motif, also called the P-loop which is common to all members of the large P-loop GTPase superfamily, coordinates ATP in the binding pocket of MinD through interactions between G13, G15, K16 and the β and γ phosphates of ATP, as well as hydrogen bonds involving T17 and T18 and the α phosphate (39–43). Two additional loops in MinD, called Switch I and Switch II, also contain residues making contact with the γ phosphate of ATP (44), illustrated in Figure 1.5.

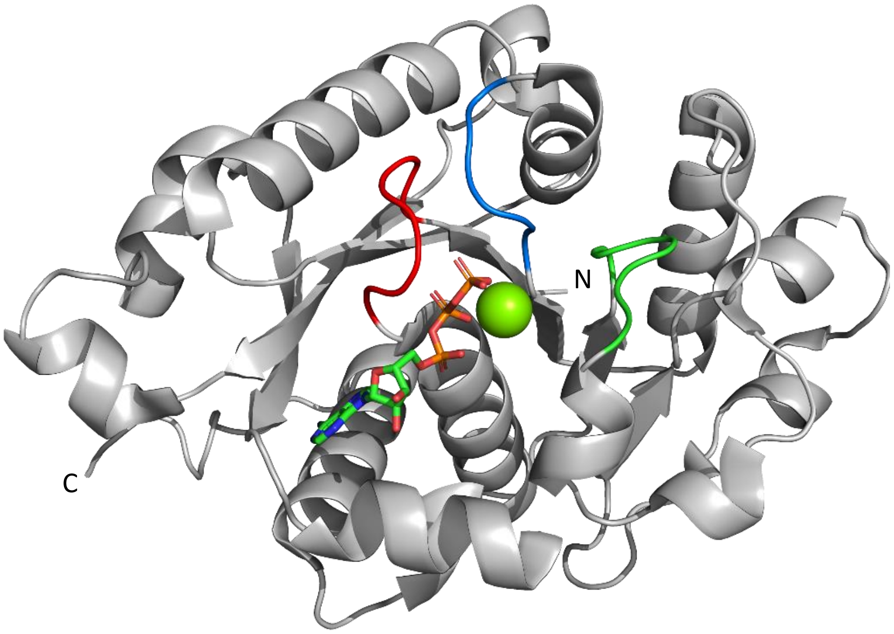

Figure 1.5 Ribbon diagram of a single ATP-bound subunit of dimeric MinD_{Ec}. A cartoon of a single subunit is depicted (PDB 3Q9L), with ATP shown as sticks colored by element and magnesium as a sphere. Loops interacting with ATP are colored: the P-loop is red, Switch I is green, and Switch II is blue.

The critical role that ATP plays in MinD dimer formation was revealed by crystal structures of ATP-bound MinD, shown in Figure 1.6. In the bound state ATP is found at the dimer interface, sandwiched between two subunits. The Walker A ‘signature’ lysine, K11 in MinD, interacts directly with the bound nucleotide when monomeric, while in the dimeric form, it changes orientation to interact with the nucleotide bound by the other subunit across the dimer interface (43). This interaction has been shown to be critical to the formation of the dimer by size exclusion chromatography of a K11A mutant which failed to form a dimer in the presence of ATP (26).

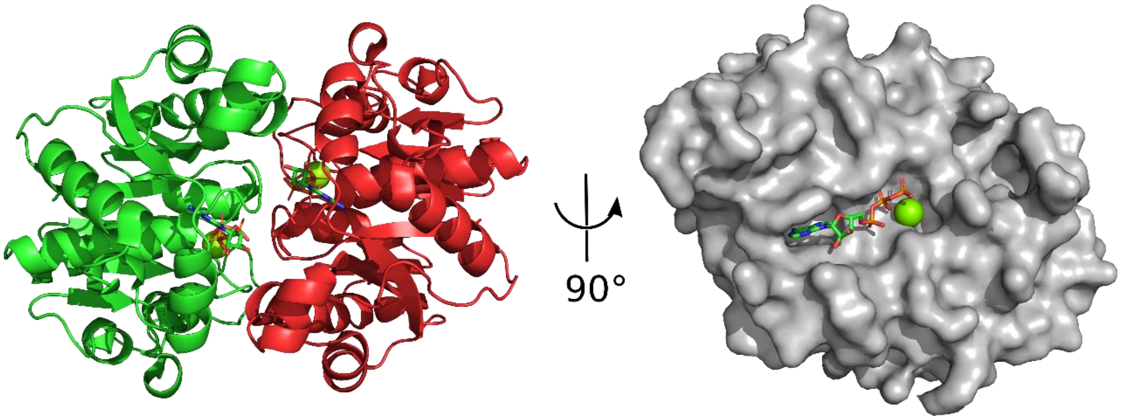

Figure 1.6 Crystal structure of MinD$_{Ec}$ in the presence of Mg^{2+} and ATP. A cartoon representation of the MinD D40A ΔC10 (PDB 3Q9L) dimer is shown, with subunits colored red or green (left). The surface representation of a single subunit on the right shows bound ATP and Mg^{2+} in a binding pocket along the dimeric interface (right). ATP is shown as sticks, colored by element. Magnesium is shown as a green sphere.

Dimerization is required for ATP hydrolysis, and is therefore a key step to the Min protein cycle of interactions. Previous studies on MinD$_{Ec}$ have seen complete conversion to a dimeric form by size exclusion chromatography in the presence of ATP (26, 28). Kinetic assays reveal stimulation of MinD ATPase activity by MinE is cooperative, suggesting some form of oligomerization of MinD prior to ATP hydrolysis (35). The small number of studies looking at dimerization of MinD$_{Ng}$ also suggest that this homologue can self-associate. Size exclusion chromatography of MinD$_{Ng}$ mutants in the presence of the non-hydrolysable analogue ATP-γ-S showed only a small population of dimer in the presence of ATP-γ-S (27). This differs from MinD$_{Ec}$ in which complete conversion to dimer was observed with ATP. Elution profiles of MinD$_{Ng}$ also suggested the presence of a dimer in the absence of ATP, which is another striking difference from previous observations with MinD$_{Ec}$ (16). Given the structural and functional similarity of MinD$_{Ng}$ and MinD$_{Ec}$, it is surprising that the dimerization properties appear to be different between the two proteins.

1.3 MinD ATPase activity

The availability of crystal structures of MinE bound to MinD, combined with mutagenesis data, give rise to a possible mechanism of stimulation of MinD ATPase activity upon interaction with MinE. The binding site of MinE on MinD is close to the nucleotide binding site, being along the dimeric interface and interacting with both MinD subunits (34). In the absence of interaction with MinE, D152 and S148 interact with the Walker A signature lysine K11, positioning the sidechain away from the bound nucleotide (34). Upon binding of ATP and dimerization, S148 interacts with N45 of the opposing subunit, liberating K11 to interact with the α and β phosphates of the bound ATP in the opposing subunit (43). Binding of MinE results in conformational changes which allow N45 to interact with the γ phosphate of bound ATP and results in ATP hydrolysis, likely by stabilizing the transition state (45). Hydrolysis is carried out by the nucleophilic attack of a water molecule which is activated by a highly conserved D40 residue (42). Interestingly stimulation of hydrolysis in one MinD subunit leads to hydrolysis in the other in a cooperative fashion, occurring even when only one MinD subunit could interact with MinE (45), however the underlying mechanism remains unclear.

Measurement of rates of hydrolysis is normally performed by monitoring the release of inorganic phosphate. Due to the cooperativity of MinD ATPase activity, analysis of initial rates is performed using the Hill equation:

$$\theta = \frac{[L]^h}{{K_{0.5}}^h + [L]^h} \qquad \text{Equation 1.1}$$

where θ is the fraction of occupied MinE binding sites in MinD, *[L]* is the concentration of ligand (MinE in this case), $K_{0.5}$ is the concentration of MinE required to reach half-maximal activity, and *h* is the Hill coefficient. During the initial phase of the reaction, the observed rate of phosphate production should be directly proportional to the fraction of occupied MinE binding sites, which can be substituted into Equation 1.1 to give:

$$\frac{v}{v_{max}} = \frac{[MinE]^h}{{K_{0.5}}^h + [MinE]^h} \qquad \text{Equation 1.2}$$

where *v* is the observed reaction rate and v_{max} is the maximum reaction rate (i.e. when all MinE binding sites are occupied) (36). From this equation the apparent affinity of MinD for MinE can be measured and used as a reporter on binding. Additionally the Hill coefficient provides insight into oligomeric behaviour, as the Hill coefficient reports on the ability of one subunit to influence another. The Hill coefficient in this reaction is reported to be in the range of 2, which is consistent with dimerization (46).

1.4 Wave formation on planar lipids

A fascinating demonstration of the dynamic oscillation of Min proteins has been shown by studies with fluorescent labeled Min proteins on planar lipid bilayers. The addition of ATP triggers the formation of ordered dynamic mesostructures which propagate in a wave-like fashion across the lipid bilayer. In these experiments, MinD forms a concentrated band along the lipid bilayer, with MinE organizing into a more concentrated zone at the trailing end of MinD (24). Total internal reflection fluorescence microscopy (TIRF) has been used to determine MinD and MinE residency time on planer bilayers (25). These experiments show that MinD accumulates on the membrane at a constant rate before plateauing at the mid-point of the wave, while MinE accumulates across the entire wave at a rate slower than that of MinD. Diffusion rates for wave-associated MinD and MinE have also been determined using TIRF on a fractionally labelled population, showing that MinE diffuses at three times the rate of MinD (25).The mechanism of this wave formation has been the subject of several efforts to reproduce the effect *in silico* using a reaction diffusion model (24, 47–49). These models generally define a mixture of two reacting species with different diffusion properties, giving rise to local variances in concentration which amplify into large-scale patterns. In these models, each component of the Min system is assigned a differential equation describing the rate of concentration change, with the condition that interactions between MinD and MinE on the membrane leads to ATP hydrolysis and release from the membrane. This process generates a local variance in MinD and MinE concentrations which, due to the altered tendency to interact with the membrane or each other in these regions, affects the rate of diffusion through the aqueous medium. These local variations are amplified into the wave patterns observed *in vitro*.

While *in silico* models of wave formation and oscillation have yielded simulations that approximate the waves observed on planar lipid bilayers, the reaction diffusion model upon which these models are based rely upon estimates of rate constants for each step in the Min cycle, the accuracy of which greatly impact the ability of these models to recapitulate various properties of Min wave formation. Many *in silico* models require the rate of nucleotide exchange to be on the order of 1 s^{-1} for dynamic pattern formation to be recreated *in silico*. However, there is no experimental evidence to support this requirement. It is therefore of interest to develop a method to measure these binding rates and determine the timescale on which this reaction is occurring. Nuclear magnetic resonance spectroscopy provides a possible solution, having the ability to measure reaction kinetics on the milli- to micro-second timescales on native substrates.

1.5 Nuclear Magnetic Resonance Spectroscopy

Nuclear magnetic resonance spectroscopy (NMR) can be used to study protein structure, dynamics, and interactions. It detects local magnetic effects around atomic nuclei which arise from their local electronic environment. Only nuclei with a non-zero quantum spin number (*I*) possess the spin angular momentum required for NMR. In the context of protein NMR, the most commonly utilized NMR-active nuclei are ^{1}H, ^{13}C, and ^{15}N. These nuclei all possess a magnetic dipole with a magnitude that is proportional to the gyromagnetic ratio of the nucleus (γ), an intrinsic property of nuclei. When placed in an external magnetic field (B_0) such as that provided by an NMR spectrometer, the magnetic dipole aligns with, and precesses around, this field. The quantum spin number dictates the number of possible orientations: ^{1}H, ^{13}C, and ^{15}N all possess $I = ½$, leading to orientations either parallel or antiparallel to the external field. These orientations are separated by an energy gap determined by:

$$\Delta E = \gamma \hbar B_0 \qquad \text{Equation 1.3}$$

where ħ is the reduced Planck constant. What is ultimately detected in an NMR experiment is the absorption of energy required to promote transition of a spin from the low-energy (parallel for ^{1}H) orientation to the higher-energy (antiparallel) orientation. Since the magnitude of the detected signal is proportional to Δ*E*, it is advantageous to use stronger external fields and nuclei with larger gyromagnetic rations, such as ^{1}H.

The energy required to stimulate these transitions is normally in the radiofrequency range of electromagnetic radiation. The frequency of absorption (v) equals the rate of procession of the dipole in the external field. While the rate of procession depends on γ and B_0, is also influenced by the small magnetic fields generated by the movement of electrons in the vicinity of the nucleus. These small fields alter the effective magnetic field experienced by the nucleus (B_{eff}) and therefore the frequency required to stimulate transitions between energy states. Contributions to the effective field arise from differences in local electron density, electrostatic environments, and chemical bonds. Therefore this difference between B_0 and B_{eff} can be used as a probe into the local chemical environment of the nucleus. Because v is proportional to B_0 the convention is to normalize v by the spectrometer magnetic field strength and report it as a chemical shift (δ):

$$\delta = \frac{v - v_{ref}}{v_{ref}} \times 10^6 \; ppm \qquad \text{Equation 1.4}$$

where v_{ref} is the frequency of a reference compound. Since local electronic contributions to B_{eff} are much smaller in magnitude relative to B_0, chemical shifts are reported in parts per million (ppm). In protein

NMR the reference frequency is that of the methyl protons in 4,4-dimethyl-4-silapentane-1-sulfonic acid (DSS).

In an NMR spectrometer the energy difference between the parallel and antiparallel spin orientations results in a thermal equilibrium population distribution with a slight excess of spins in the lower energy configuration. This gives rise to a bulk magnetization vector aligned parallel to the external magnetic field comprised of the small excess of spins that all precess around the axis of B_0 with angular momentum defined by the Larmour frequency:

$$\omega_0 = 2\pi v \qquad \text{Equation 1.5}$$

Application of a radiofrequency pulse perpendicular to the external field matched to ω_0 applies to a torque to the bulk magnetization vector that rotates it away from the axis of the external field. The length and power of the pulse dictates the angle of rotation, making it possible to cause a 90° rotation that places the bulk magnetization vector in the transverse plane. The precession of this vector about B_0 can be detected in the spectrometer by a receiver coil oriented perpendicular to the axis of B_0 that can sense how the magnitude of the projection of the magnetization vector along the receiver coil axis changes over time. This time-dependent change in signal intensity gives rise to an oscillating signal known as a free induction decay (FID). The frequency of the oscillation corresponds to the frequency of absorption, which can be obtained using a Fourier transform. The peak width at half height of the resulting spectra, a result of the rate of decay of the FID, is dictated by T_2 relaxation (explained later). This gives rise to an NMR spectrum where peaks appear at the absorption frequency of each spin, with an intensity that reflects, in part, the population of spins in that particular local chemical environment.

A useful property of NMR-active nuclei is the ability for nuclear spins to interact through bonds in a process known as J-coupling. This coupling can be used to transfer magnetization from an excited spin to its bonded neighbour(s) to indirectly measure chemical shift of these nuclei in a multidimensional NMR experiment. This technique allows peaks to be separated into more than one dimension, thereby reducing overlap, and chemical shifts of bonded nuclei to be correlated, which is critical for the process of chemical shift assignment.

1.1.1 Spin relaxation

Due to the relatively small energy difference between the parallel and antiparallel orientations, the bulk magnetization vector is small in magnitude, making NMR an insensitive technique. Compounding this issue is spin relaxation, which is the process by which NMR signals decay over time. There are two types of relaxation that can affect the sensitivity of an NMR experiment: 1) Longitudinal relaxation (T_1), which is the process by which the population of excited spins returns to its equilibrium distribution, and; 2) Transverse relaxation (T_2), which is the gradual loss of coherence (i.e. dephasing) of the bulk magnetization vector. Both T_1 and T_2 relaxation influence signal intensity, while T_2 relaxation also affects peak linewidths. Relaxation arises from changes in the effective magnetic field that arise from molecular tumbling in solution, with dipole-dipole coupling and chemical shift anisotropy (CSA) being the two main sources of these changes. When these fluctuations in local magnetic fields experienced by a spin occur at frequencies that can induce transitions (e.g. the Larmour frequency) excited spins can return to the ground state which ultimately allows the equilibrium distribution of spins to be restored. Large molecules, like proteins, undergo slow molecular tumbling rates in aqueous solution, which limits the effectiveness of T_1 relaxation, making it necessary to use longer delays between each experiment to allow the spins to return to equilibrium. In addition, slow tumbling rates lead to rapid loss of coherence, which causes short T_2 times and broad linewidths.

1.1.2 Measuring protein dynamics with NMR

While NMR is conventionally considered useful for the study of stable complexes, techniques exist which allow the measurement of protein conformational dynamics over a wide range of timescales. These measurements depend on the rate of the dynamics relative to the NMR timescale. If a spin is in a part of the protein that samples more than one state, but exchanges between states at a fast rate (i.e. faster than milliseconds), transitions between the two states occur while the signal is being recorded that give rise to a single peak at the population-weighted average chemical shift between the two species. For example, in the case of methyl protons only one peak is detected, since rotation about the methyl group axis occurs on the picosecond to nanosecond timescale averages the local chemical environment of all thee protons. In contrast, when a dynamic process is slower (i.e. milliseconds to seconds) the chemical shift of each state is independently measured, as the sample being studied is comprised of a mixed population of both states that does not significantly interconvert during acquisition of the NMR signal. Under circumstances when the rate of exchange is less than the difference in absorption frequency of the two states (Δv), each state gives rise to a distinct peak with an intensity that reflects the population of the state. When exchange rates are close to the difference in absorbance frequencies, peaks tend to broaden and occur at chemical shifts that approach the average peak position that is seen in the fast limit of exchange. The exchange limit k_c (50) where the two states give rise to a single peak (the coalescence point) can be calculated using:

$$k_c = \frac{\pi \times \Delta v}{\sqrt{2}} \cong 2.22 \times \Delta v \qquad \text{Equation 1.6}$$

When exchange occurs on the millisecond to second range it is possible to use ZZ-exchange experiments to measure the rate of exchange (51). In this process a delay is added in a ^{1}H – ^{15}N HSQC type of experiment which permits transitions between the two states to occur. This gives rise to new peaks, termed cross-peaks, with the ^{1}H chemical shift of one species but the ^{15}N chemical shift of the other. The volume of these peaks is related to the duration of the delay and the rate of exchange between states. By measuring these peak volumes for experiments run with various delay times, the rates of exchange can be determined. However, this technique requires that populations of the two states be large enough to be detected as separate species in the HSQC experiment, which may not always be the case. In cases where exchange rates are on the same order of magnitude as k_c, (usually on the millisecond to microsecond time scale) T_2 relaxation becomes faster, leading to peak broadening. The contribution of these exchange processes to T_2 can be measured in what is known as a CPMG experiment (52). Similar to the ZZ-exchange experiment, a delay is added in the standard ^{1}H – ^{15}N HSQC experiment, although in this case, a series of pulses are applied that serve to refocus magnetization that has dephased due to exchange between states. As the frequency of these pulses is increased, the contribution of exchange to T_2 relaxation is minimized. Peak volumes are measured and plotted as a function of the pulse frequency in this delay, allowing exchange rates to be measured so long as the population of the minor state is at least 5% of the total population.

1.6 NMR spectroscopy of large proteins

1.6.1 TROSY

Since MinD is 30 kDa protein, with a potential to form a 60 kDa dimer when bound to ATP, it is necessary to use solution NMR methods that are geared towards the study of large proteins. One of these is the Transverse Relaxation Optimized Spectroscopy (TROSY) experiment (53). This experiment takes advantage of destructive interference between relaxation caused by dipole-dipole versus chemical shift anisotropy. In a ^{1}H-^{15}N version of this experiment, there is no decoupling of the strong through-bond interaction that occurs between the amide proton and nitrogen which, in a normal HSQC, would give rise to a quartet of peaks for every amide proton in the protein: a doublet in the 1H dimension, and a doublet in the ^{15}N dimension, each separated by the ^{1}H-^{15}N J-coupling constant and each having different relaxation properties. In the TROSY version of this experiment, only the narrowest peak in the quartet that results from the destructive cancellation of dipole-dipole and chemical shift anisotropy relaxation is isolated. The enhancement in peak resolution and sensitivity is larger at higher magnetic field strengths and also increases with the size of the system being studied.

1.6.2 Deuteration

Additional contributions to T_2 relaxation of amide protons results from longer-range dipole-dipole interactions with proximal ^1H nuclei. To reduce relaxation by this mechanism, it is possible to substitute protons at non-exchangeable sites with deuterium, an isotope of hydrogen with a significantly lower gyromagnetic ratio than that of ^1H. To achieve this, bacteria expressing the protein of interest are cultured in a D_2O-based media with deuterated glucose to give close to uniform incorporation of deuterium. Even if a D_2O culture is grown with ^1H-glucose, significant enhancements in relaxation properties can be realized. This is possible as during many amino acid biosynthetic pathways, the proton on the alpha carbon originates from the solvent, which in a deuterium-containing solvent would be substituted with deuterium. This eliminates one of the largest sources of dipole-dipole relaxation, giving rise to significant improvements to spectral sensitivity and resolution.

1.6.3 Temperature

The rate of tumbling in solution has been highlighted as a critical factor to the success of an NMR experiment. Therefore to improve spectra of large proteins, it is possible to increase tumbling rates by acquiring spectra at elevated temperature, so long as the protein remains stable under these conditions. The rate of molecular tumbling can be characterized by its correlation time (τ_c), defined as the time taken to rotate through 1 radian, which is inversely proportional to temperature:

$$\tau_c = \frac{4\pi\eta r^3}{3kT} \qquad \text{Equation 1.7}$$

where η is the solution viscosity coefficient, r is the radius, k is the Boltzman constant, and T is the sample temperature. Therefore by increasing sample temperature, the correlation time can be decreased (i.e. tumbling rates increase), resulting in faster T_1 and slower T_2 relaxation.

1.6.4 Backbone chemical shift assignment

When using NMR to study local effects in a protein of interest, it is essential to be able to identify the residues that give rise to each peak. This requires that peaks in the NMR spectrum be assigned to the atoms in the protein in a process known as chemical shift assignment. This is achieved through a series of related 3D triple-resonance experiments, where correlations are obtained for backbone amide proton, amide nitrogen, Cα/β, and/or carbonyl resonances. These multidimensional experiments rely on

J-coupling interactions between spins that provide a mechanism to transfer magnetization from excited nuclei to adjacent, covalently bonded nuclei.

The goal of backbone assignment is to be able to link adjacent residues through shared correlations of specific nuclei. For this purpose, a series of experiments based on the amide $^{1}H - ^{15}N$ correlation is collected that transfers magnetization from amide protons to the Cα and/or Cβ carbon atoms where the chemical shift is recorded before the magnetization is returned to the amide proton for detection. This gives rise to correlations between the amide ^{1}H and ^{15}N atoms, and Cα/Cβ atoms from both the preceding residue, and the same amino acid. This allows amide peaks from adjacent residues to be identified, since they should show correlations with the same Cα/Cβ atoms. One commonly used experiment is the HNCA, where correlations to the Cα atom from the preceding residue and same amino acid are recorded (54). The resulting spectrum can then be analyzed as strip plots, where the 3D spectrum is viewed as a series of 2D $^{1}H - ^{13}C$ planes centered on the correlation's ^{15}N position. These peaks can be ordered into continuous fragments and then matched to the protein sequence by comparison with a database of standard ranges of chemical shifts for each amino acid.

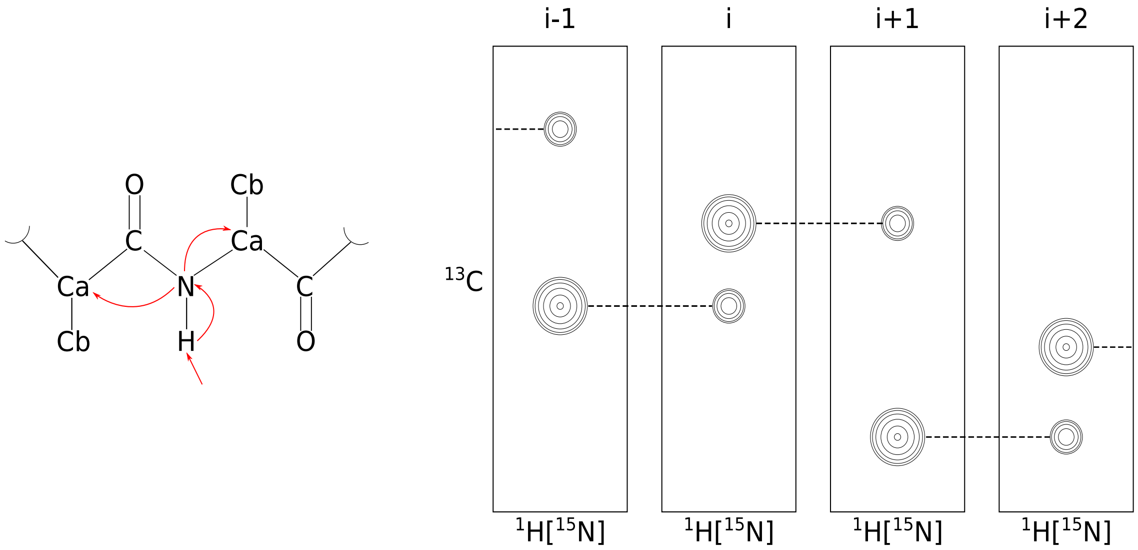

Figure 1.7 Schematic representation of an HNCA experiment. Magnetization transfers along the protein backbone are depicted (left) as are strips of the resulting spectrum (right). An amide N-H group from each residue is represented in a strip, with two correlations originating from the preceding Cα (typically a weaker peak) and from the same residue (typically a stronger peak). Residue positions relative to reference (i) are listed at top.

The longer the fragment, the easier it is to assign it to a unique region of the protein sequence. If a fragment is shorter, however, there may be multiple possible assignments that are consistent with the chemical shifts, making it necessary for correlations of other atoms to be acquired to achieve a unique assignment. A typical experiment set for backbone assignment consists of HN(CO)CACB (55, 56) which provide correlations for the preceding residue Cα/Cβ atoms, and HNCACB (57, 58) which provides correlations for both the current and preceding residue Cα/Cβ atoms. In larger proteins like MinD it becomes necessary to run additional experiments (e.g. HNCB (58), HN(CA)CO (59)) which provide unique correlations for each atom type (i.e. only the preceding residue, only Cβ), and include correlations for carbonyl atoms.

The assignment of chemical shifts to specific atoms in the protein backbone offers insight into the secondary structure since the dihedral angles imposed by different secondary structures result in characteristic shielding or deshielding effects (60). Therefore the propensity for any given residue to participate in helical or beta-stranded secondary structure can be estimated by comparing the assigned chemical shift of backbone nuclei to values obtained for random coils in a process called secondary shift calculation (61).

1.6.5 Selective labelling

The large number of nuclei in a protein result in a complex convolution of signals. Combined with poor spectral resolution normally seen with large proteins, this can lead to many overlapping signals which are hard to resolve. It is possible to reduce the number of signals by not uniformly labelling the protein with NMR active isotopes. This can be achieved by culturing with isotopically-labelled amino acids or their precursors, which the bacteria preferentially incorporate into expressed proteins if added at the time of induction. However the prohibitive cost of labelled amino acids and precursors compared to uniform isotopic labelling make this technique unattractive. It is however quite economical to selectively un-label residues instead. The same process applies: culturing in a isotopically-labelled media, with the addition of unlabelled amino acids or precursors. These, being preferentially incorporated, will result in silencing of signals arising from residues of a specific amino acid.

Unfortunately the biosynthesis pathways for various amino acids in common expression systems such as *E. coli* contain many reversible processes which can result in 'scrambling' of labels into other amino acids. One such example is Val, which can be reverted to 2-oxoisovalerate that eventually becomes Leu (62). This process makes it very challenging to only label one amino acid at a time, so many protocols involve labelling of groups of amino acids simultaneously which have a propensity to scramble (63–66). Research into scrambling propensity in *E. coli* BL21(DE3) expression systems has been performed by adding one unlabelled amino acid at a time to an isotopically labelled growth media, and comparing peak intensities of known residues in the resulting ^{1}H – ^{15}N HSQC spectrum (67). Amino acids such as Arg and Lys demonstrate no significant ^{15}N scrambling and are quite numerous in the sequence of MinD, making them attractive targets for unlabelling efforts.

1.7 Thesis objectives

Many models of Min protein oscillation require that nucleotide exchange occur on the millisecond to second timescale, an assumption that has never been experimentally verified. Solution NMR has the potential to provide an answer to this question, so long as assigned spectra can be obtained. In this thesis I describe the progress made towards this goal by undertaking the backbone chemical shift assignment of MinD$_{Ng}$. Since we were interested in characterizing changes in NMR spectra that arise from nucleotide binding, the oligomeric state of MinD$_{Ng}$ in the presence and absence of nucleotide was also characterized. Results from this thesis lay the groundwork for future studies to measure rates of nucleotide exchange by NMR to determine whether nucleotide exchange rates are slow enough to explain oscillation of Min proteins *in vivo*.

2 Materials and Methods

2.1 Transformation

Competent *E. coli* BL21(DE3) cell stocks (Novagen) were divided into 40µL aliquots and flash-frozen in liquid nitrogen. Aliquots were stored at -80°C until use.

Transformation was performed using standard protocols (68). One aliquot of competent cells was thawed on ice, followed by the addition of 1ng/µL plasmid DNA. Aliquots were mixed by flicking, then left to incubate on ice for 30 minutes. Following incubation, the aliquot was subjected to heat shock at 42°C for 90 seconds and immediately returned to ice for 2 minutes. 200µL of sterile LB media was added to the aliquot which was then incubated at 37°C for 1 hour, followed by plating on a kanamycin-selective LB agar plate. This plate was left to grow overnight at 37°C.

2.2 Overexpression of MinD

MinD proteins were prepared and purified as previously described (69). One transformed colony was used to inoculate 80mL of prepared M9 media (57mM Na_2HPO_4, 22mM KH_2PO_4, 8.5mM NaCl, 1mM $MgSO_4$, 0.1mM $CaCl_2$, 50µg/mL kanamycin, 0.1% (w/v) NH_4Cl, 0.3% (w/v) D-glucose, 0.1% (w/v) LB broth), which was then incubated overnight at 37°C while shaking at 220rpm. 800mL of prepared M9 media was inoculated by the addition of the entire 80mL pre-culture, followed by growth at 37°C while shaking at 220 rpm. Once the OD_{600} reached 0.45 protein expression was induced by the addition of 0.5mM IPTG (BioShop). The culture was grown at 16°C for 18 hours while shaking at 220rpm. Cells were harvested by centrifugation at 4800xg, 4°C for 15 minutes. Cell pellets were recovered and stored at -20°C until use.

2.2.1 Isotope Labelling

Stock of 10% $^{15}NH_4Cl$ or 30% $^{13}C_6$-D-glucose (Aldrich) were prepared in ddH_2O and sterilized by a 0.22µm filter. These were used to prepare the M9 media, being substituted for natural abundance NH_4Cl or D-glucose as required.

2.2.2 Selective Unlabelling

Overexpression was carried out with ^{15}N-labelled ammonium chloride as above until induction. 0.1g/L of the targeted unlabeled (^{14}N) amino acid (BioShop) was added simultaneously with 0.5mM IPTG. The culture was then grown at 37°C for 3 hours before harvesting.

2.3 Deuteration

2.3.1 Optimization of Protein Expression

Competent *E. coli* BL21(DE3) cells were transformed as above. One transformed colony was used to inoculate 80mL of LB broth with 50µg/mL kanamycin. This culture was grown at 37°C overnight while shaking at 220rpm. The following morning the OD_{600} of this culture was measured and used to determine the volume of culture required to yield a starting OD_{600} of 0.1 in an 80mL M9 culture that was then incubated at 37°C, 220rpm for 3 hours. The remaining LB culture was stored at room temperature for this period.

An appropriate volume of the culture grown in M9 media or LB media was used to inoculate 80mL of D_2O-based M9 media to yield a starting OD of 0.1. Cells were transferred by centrifuging the aliquot of culture at 5000xg for 5 minutes and resuspending the pellets in a minimum amount of D_2O-M9 media. A third, H_2O-based prepared M9 media culture was inoculated with 10% (v/v) M9 culture to simulate the normal culturing procedure.

The three cultures were grown at 37°C, 220rpm for 4 hours. Once the OD_{600} surpassed 0.45, a 1mL sample of each culture was taken. The remaining culture was induced with 0.5mM IPTG. After an 18-hour overnight incubation at 16°C, 220rpm another 1mL sample of each culture was taken. Culture aliquots were centrifuged at 16 000xg for 1 minute, then 100µL of SDS-PAGE loading buffer was added to the pellets. The samples were frozen at -20°C until analysis by SDS-PAGE.

2.3.2 Expression of ^{2}H, ^{13}C, ^{15}N-Labelled MinD

Competent *E. coli* BL21(DE3) cells were transformed as above. One transformed colony was used to inoculate 80mL of LB broth with 50µg/mL kanamycin. This culture was grown at 37°C overnight while shaking at 220rpm. Two flasks containing 80mL of ^{15}N,^{13}C M9 media were inoculated to a final OD_{600} of 0.1, and grown at 37°C, 220rpm to a final OD_{600} >0.5. The two 80mL cultures were centrifuged at 5000xg for 5 minutes, then the pellet resuspended in a small volume of D_2O-based prepared M9 media which was then transferred into 800mL of 0.22 µm filter-sterilized ^{15}N,^{13}C-labelled M9 media prepared in D_2O (Spectra Stable Isotopes). The starting OD_{600} of the 800mL culture was 0.1. It was allowed to reach an OD_{600} of 0.45 by incubation at 37°C, 220rpm, at which point expression was induced with 0.5mM IPTG. The culture was grown for 18 hours at 16°C, 220rpm before being harvested by centrifugation at 4800xg, 4°C for 15 minutes. Pellets were stored at -20°C until use.

2.4 Purification of MinD

Purification was performed as previously described (36). One cell pellet obtained from 400mL of culture was resuspended in 15mL of Lysis Buffer (250mM NaCl, 10mM imidazole, 50mM Tris pH 8.5, 1mg/mL benzamidine) and incubated on ice on a rocking platform for 30 minutes. The cell suspension was then lysed twice by an EmulsiFlex-B15 French press homogenizer (Avestin) with 80 psi valve pressure. This lysate was then centrifuged at 16 000xg, 4°C for 20 minutes.

The supernatant was added to a column containing 5mL of Ni-NTA resin (Qiagen) that had been equilibrated with 10mL Lysis Buffer. After a 5-minute incubation the supernatant was allowed to flow through, and then the column was washed with 50mL Lysis Buffer. The column was then washed with 50mL of Lysis Buffer containing 20mM imidazole. At the completion of these washes the flow was stopped and the column incubated with 10mL of Lysis Buffer containing 500mM imidazole. After 5 minutes the flow was allowed to resume, and the eluate collected. EDTA pH 8.5 was added to a final concentration of 0.5mM, and TCEP-HCl pH 7.2 to a final concentration of 1mM.

The eluate was concentrated to 2mL by centrifugation at 4000xg, 4°C using Amicon Ultra concentration devices with a 30kDa (full-length MinD) or 10kDa (MinD ΔC10) molecular weight cut-off. Samples were then subjected to size exclusion chromatography on a Superdex SP75 10/300GL column (GE Healthcare) equilibrated with 40mL Exchange Buffer (100mM NaCl, 0.2mM EDTA, 50mM Tris pH 8.5). Chromatography was performed at 0.5mL/min on an AKTA FPLC (Amersham Biosciences) with absorbance at 280nm monitored and 0.5mL fractions collected.

2.5 Measurement of protein concentration

A 14mg/mL stock of bovine serum albumin (BSA) (Fisher) was used to prepare standards for use in a bicinchoninic acid (BCA) assay (70). Dilutions of 25, 50, 100, 200, 400, 500, 750, and 1000µg/mL BSA were prepared in ddH_2O and stored at 4°C before use. 1mL of 50 parts Reagent A (200mM sodium carbonate, 120mM sodium bicarbonate, 10mM sodium tartrate, 0.1M sodium hydroxide and 30mM BCA) to 1 part Reagent B (4% $CuSO_4$) was added to 50µL of each protein concentration standard or the sample of unknown concentration and then incubated at 37°C for 30 minutes. After incubation, absorbance at 562nm was recorded with an Ultrospec 2100 Pro spectrophotometer (Biochrom) for each standard sample, plotted against the concentration, and fit to a line using linear regression. The equation of the best-fit line was used to determine the concentration of unknown samples.

2.6 SDS-PAGE analysis

0.75mm gels were cast with a 12% resolving phase (12% acrylamide, 225mM Tris pH 8.8, 0.05% SDS, 0.15% ammonium persulphate, 0.02% TEMED), and a 5% stacking phase (5% acrylamide, 25mM Tris pH 6.8, 0.02% SDS, 0.02% ammonium persulphate, 0.02% TEMED).

SDS-PAGE was performed using the Laemmli procedure (71). Samples to be analyzed were stored at -20°C with loading buffer (125mM Tris pH 6.8, 20% glycerol, 4% SDS, 0.01% bromophenol blue and 2% 2-metacaptoethanol). Samples were incubated for 5 minutes in boiling water before 20µL of sample and 3µL EZ-Run Prestained Rec Protein Ladder (Fisher BioReagents) were loaded onto the gel.

Gels were run in a Mini-PROTEAN electrophoresis cell (Bio-Rad) for 50 minutes at 180V in running buffer (25mM Tris pH 8.5, 192mM glycine, 0.1% SDS). Gels were then stained for one hour with Coomassie Blue (50% methanol, 10% acetic acid, 0.1% Coomassie Brilliant Blue) on a rocking platform. Excess stain was rinsed off, followed by incubation in destaining solution (50% methanol, 10% acetic acid) for 30 minutes on a rocking platform, at which point the solution was drained and the gel incubated in another volume of destain solution for 1 hour. Gels were stored in ddH_2O until visualization by flatbed scanner.

2.7 Preparation of small unilamellar vesicles

Small unilamellar vesicles were prepared immediately before use in accordance with established protocols (72). 10mg *E. coli* total lipid extract (Avanti) was dissolved in ~200uL of chloroform in a glass test tube and subsequently dried under a stream of argon gas. The film was resuspended to give a concentration of 10mg/mL in Reaction Buffer (50mM KCl, 25mM Tris pH 8) by pipetting. The suspension was withdrawn into a 250µL gas-tight syringe and incubated at 50°C for 5 minutes, then extruded through a 1µM membrane 21 times using an Avanti Mini-Extruder. The sample was extruded again through a 0.1µM filter, which was then ready for immediate use.

2.8 Malachite green assay for detection of phosphate

One volume of 4.2% (w/v) NH_4MoO_4 in 4M HCl was mixed with three volumes of 0.045% (w/v) malachite green (Bioshop) and incubated at room temperature for an hour on a shaking platform. This stock solution was filtered with a 0.22µm filter and then stored at 4°C until use. Prior to use in an ATPase assay 65 parts ddH_2O was added to 20 parts of this stock solution along with Tween-20 to a final concentration of 0.15% (v/v). This solution was incubated at room temperature for 30 minutes on a rocking platform before use.

A standard curve was prepared for each stock solution using KH_2PO_4 standards ranging in concentration from 1.5mM to 25μM in ddH_2O. 15μL of each standard was mixed with 85μL of dye in a polystyrene 96 well plate and incubated at room temperature for 15 minutes before recording the absorbance at 620nm. Absorbance was plotted against phosphate concentration and linear regression used to determine the equation of the best-fit line, which was then used to convert absorbance readings into phosphate concentrations for samples of unknown phosphate concentrations in the ATPase assay.

2.9 ATPase assay

1mM ATP was added to reaction mixtures containing 65mM Tris-HCl pH 8.2, 80mM NaCl, 50mM KCl, 0.16mM EDTA, 5mM $MgCl_2$, 0.5mg/mL *E. coli* SUVs, 2.7μM MinD, and varying concentrations of MinE. The first 35μL sample was taken 15 minutes after the addition of ATP to the reaction, then every 3 minutes thereafter until the reaction had run for 30 minutes. Each aliquot was immediately transferred to a boiling water bath and left for 1 minute inactivate MinD. 15μL of each sample was added to 85μL malachite green dye in a 96-well microplate and incubated at room temperature for 15 minutes. Absorbance was read at 620nm using a SpectraMax Plus 384 Microplate Reader (Molecular Devices) and plotted against elapsed reaction time. Reaction rates were determined from the slope of the best fit line determined by linear regression, then converted into units of phosphate concentrations using the slope of the phosphate standard curve. These rates were then fit to Equation 1.2 using a least squares regression.

2.10 Oligomerization state determination

The molecular weight of MinD samples was estimated by size exclusion chromatography using either a Superdex SP75 10/300GL or Superdex SP200 10/300GL column (GE Healthcare). 0.5mL aliquots of 40μM WT or 6μM D40A MinD in NMR Buffer with 5mM $MgCl_2$ and either no nucleotide, 1mM ADP, or 1mM ATP were injected on a column equilibrated with NMR buffer containing 5mM $MgCl_2$ and, as required, 1mM nucleotide. Samples were run at 0.5mL/min with 0.5mL fractions collected and absorbance at 280nm monitored. Fractions were analyzed by SDS-PAGE, and gel band intensities integrated by ImageJ (73). Relative band intensities were plotted against the center of the elution volume of the fraction. Deconvolution of elution profiles monitored by absorbance at 280nm was performed using Fityk (74).

Multi-angle light scattering was performed using an AKTA Pure FPLC (GE Healthcare) equipped with a Viscotek VE3580 RI Detector and Viscotek SEC-MALS 20 (Malvern Instruments). 0.5mL of sample (1mg of protein) was loaded on a Superdex SP75 10/300GL column equilibrated with exchange buffer at a flow rate of 0.5mL/min. The SEC-MALS/RI data was collected and analyzed with Viscotek OmniSEC BIO 4.7 (Malvern Instruments). The MALS detector was normalized using the monomeric signal of BSA. Molar mass was determined using a refractive index increment (dn/dc) of 0.185mL/g.

2.11 Circular dichroism spectroscopy

Purified protein was concentrated to below 1mL, washed twice with 10x volume of CD Buffer (130mM NaCl, 10mM Tris pH8.5), concentrated to 1mL, then final protein concentration was determined by BCA assay. 10µM protein in a quartz cuvette was analyzed using a Jasco J-1500 spectrophotometer. Spectra were recorded at 25°C from 250 to 200nm. 8 scans were recorded at 10nm/min with 32s data integration time. A buffer blank was recorded and subtracted from resulting spectra.

2.12 NMR spectroscopy

Samples were concentrated to 1mL by centrifugation at 4000xg, 16°C in an Amicon Ultra concentration devices with a 30kDa (full-length MinD) or 10kDa (MinD ΔC10) molecular weight cut-off. Samples were then diluted 10-fold with NMR Buffer (25mM Tris pH7.2, 50mM NaCl, 1mM TCEP, 0.1mM EDTA, 0.2mM Benzamidine, 0.02% NaN_3) and concentrated again to below 1mL. This process was repeated for a total of two times. The final sample was concentrated to 300µL (for use with shaped tubes) or 400µL (for use with Shigemi tubes), to which D_2O (Aldrich) was added to a final concentration of 10% (v/v). All spectra were acquired at 298K using a 600MHz Avance III spectrometer (Bruker) equipped with a triple-resonance cryoprobe at the University of Ottawa NMR Facility. Backbone assignment experiments were carried out on a uniformly ^{13}C,^{15}N-labelled, deuterated 1.4mM sample of MinD ΔC10 in NMR buffer. ^{1}H, ^{15}N, and ^{13}C backbone chemical shifts were assigned using ^{15}N TROSY, TROSY-like HNCO, HN(CA)CO, HNCA, HN(CO)CA, HN(CA)CB, and HN(COCA)CB spectra processed by NMRPipe (75) and analyzed with NMRView (76). To maintain a stable lock over the duration of the experiments it was necessary to disable auto-shimming and decrease ^{2}H decoupling pulse power to -0.97dB for 358.6µs.

2.13 Nucleotide binding affinity measurements

A ^{1}H – ^{15}N TROSY spectrum of a 150µM sample of uniformly ^{15}N-labelled MinD ΔC10 in NMR buffer with 5mM $MgCl_2$ was recorded first in the absence of nucleotide, and again with increasing nucleotide concentrations. In the first round, concentrations were increased 10-fold in each iteration, ranging from 100pM to 10mM. Based on the results of this experiment, an appropriate concentration range for higher frequency sampling was identified and the experiment was repeated with an 800µM sample, wherein 21 concentrations of nucleotide centered around the approximate K_D were tested.

Populations of bound and unbound MinD ΔC10 were estimated by integrating four reporter peak volumes with NMRPipe. These were plotted as a function of nucleotide concentration and fit to a binding isotherm using a least-squares regression.

3 Results

3.1 Overexpression and purification of MinD

MinD was overexpressed with a C-terminal hexahistadine tag in E. coli BL21(DE3) competent cells. and isolated by nickel affinity chromatography. Samples were taken at various points during the purification process to monitor purification efficacy. As shown in the Coomassie Blue-stained gel of fractions taken at various points during expression and purification (Figure 3.1), a band corresponding to a species with ~30 kDa molecular weight, which corresponds to the expected mass of MinD, appears once expression is induced and is isolated by the end of the purification process, yielding less than 1mg protein per liter culture with a purity of >95%.

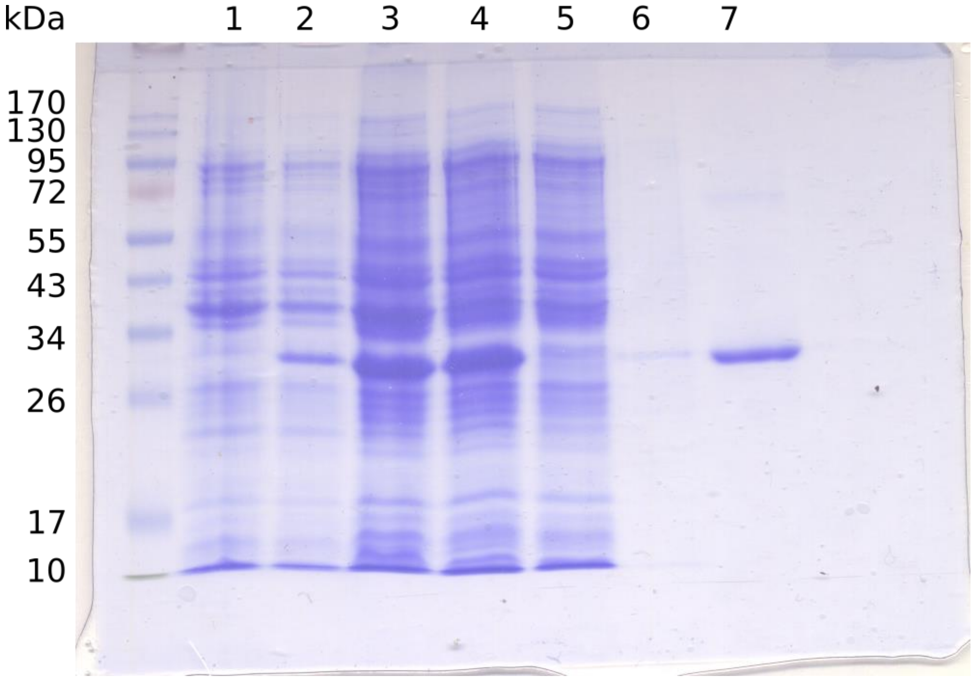

Figure 3.1 Purification of MinD D40A monitored by Coomassie Blue-stained SDS-PAGE. Samples were taken of 1) cell culture before; and, 2) after induction of expression; 3) whole-cell lysate; 4) the soluble fraction of the lysate; 5) nickel column flow-through; 6) low imidazole nickel column wash; 7) nickel column elution.

3.2 Stimulation of MinD ATPase activity

As part of the Min cycle, membrane-bound MinD hydrolyzes ATP upon stimulation by MinE. Since the x-ray crystal structure of MinD used an alanine mutant of a critical aspartic acid residue in the catalytic site, namely Asp40, the analogous mutation was made in MinD_{Ng}. To confirm that the ATPase activity of this mutant was eliminated, ATP hydrolysis rates were measured for both wild-type and D40A MinD by monitoring the production of inorganic phosphate. As can be seen in Figure 3.2, wild-type MinD displayed a cooperative kinetic profile while MinD D40A was unresponsive to stimulation by MinE, confirming its loss of ability to catalyze ATP hydrolysis.

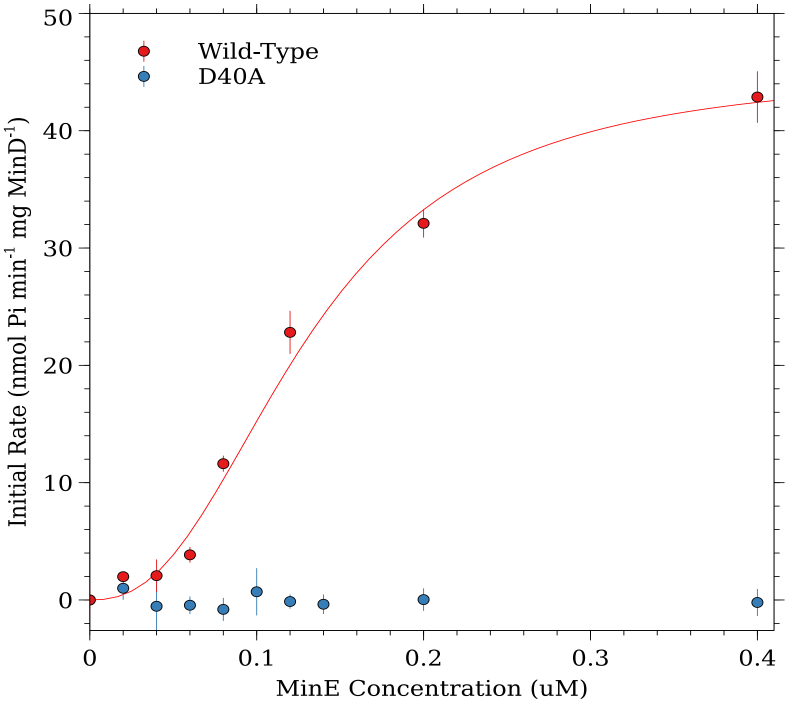

Figure 3.2 MinE-stimulated MinD-catalyzed ATP hydrolysis rates for wild-type and D40A MinD. Fit of measured rates to the Hill equation are shown for wild-type MinD.

3.3 ^{1}H – ^{15}N HSQC spectrum of MinD

To test the feasibility of NMR experiments, a ^{1}H – ^{15}N HSQC was collected of uniformly ^{15}N-labelled MinD. In HSQC experiments the expected number of peaks is approximately equal to the number of non-proline residues in the protein (i.e. 273). As can be seen in Figure 3.3, while the peaks are well dispersed, only about one third of the expected peaks were observed. Additionally, the resolved peaks were of low intensity and quite broad. Given the low levels of expression obtained for MinD (less than 1mg per liter of culture) and the poor solubility at neutral pH for amide-proton-detected NMR experiments, it was not possible to use full-length MinD for high resolution NMR studies.

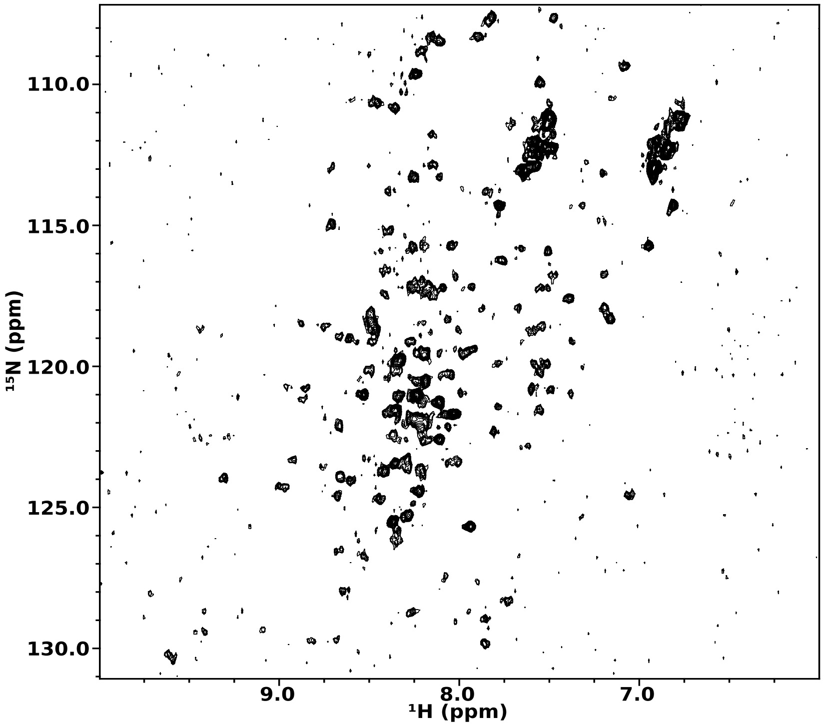

Figure 3.3 ^{1}H – ^{15}N HSQC of uniformly ^{15}N-labelled MinD at 25°C, pH 7.2, with a MinD concentration of 30 μM.

3.4 ^{1}H – ^{15}N HSQC spectrum of MinD D40A

An inactive mutant of MinD, namely D40A, was subsequently tested for amenability for structural studies, as it had been observed to exhibit both higher expression levels and improved solubility compared to wild-type MinD. To this end, a ^{1}H – ^{15}N HSQC spectrum of MinD D40A was recorded and compared to the wild-type spectrum (Figure 3.4). A considerably larger number of peaks was observed (~170) compared to the spectrum with wild-type MinD. Many of the peaks in this spectrum had chemical shifts that were identical to those of the WT protein, suggesting that MinD D40A is structurally analogous to wild-type MinD. While these peaks were still relatively broad, their intensities were much higher than those seen in the wild-type spectrum, and therefore we switched our focus to the study of the D40A mutant in subsequent NMR studies.

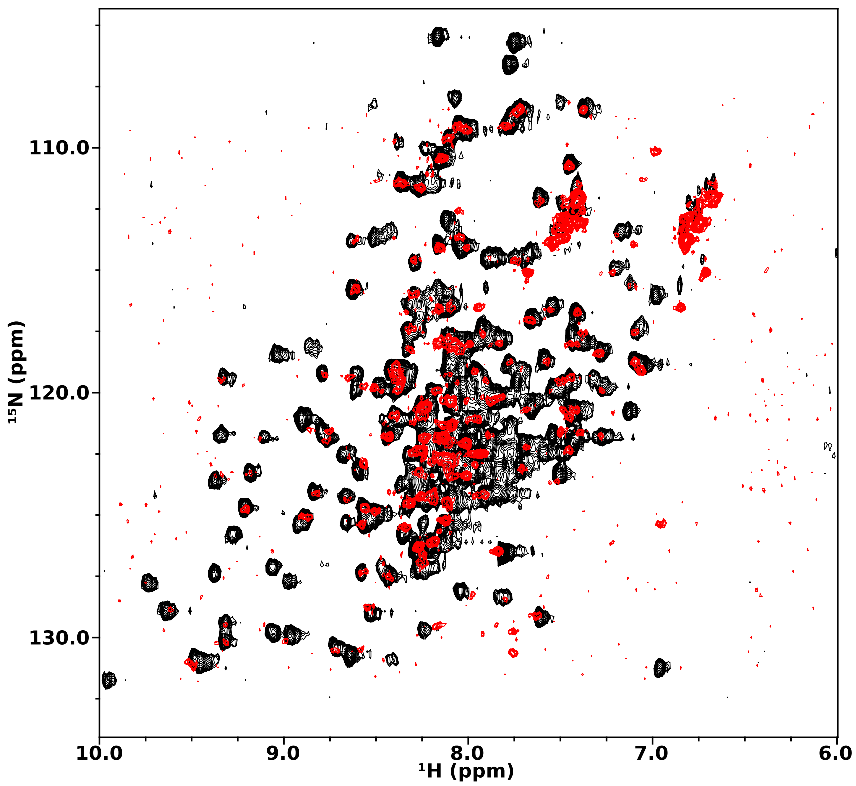

Figure 3.4 ^{1}H – ^{15}N HSQC of uniformly ^{15}N-labelled MinD wild-type (20μM, red) over MinD D40A (50μM black). Spectra were recorded at 25°C, pH 7.2.

3.5 Investigation of nucleotide binding by NMR

To explore the effect of nucleotide binding on the NMR spectrum of D40A MinD, a series of ^{1}H – ^{15}N HSQC spectra were acquired in the presence of 1mM ADP or ATP, (Figure 3.6). In both cases a large proportion of peaks showed large chemical shift changes upon introduction of nucleotide, however, peak intensities were significantly weaker in these spectra, with peak broadening being apparent. In addition, the sample that was incubated with ATP was found to form a precipitate over the course of the experiment, suggesting a loss of solubility. Perhaps most surprising was the similarity between spectra of the ADP and ATP bound states (Figure 3.5), as ATP should induce the formation of a dimer (27, 28) that would significantly change the local chemical environment of a large number of residues at the dimeric interface. For this reason, it was necessary to investigate the effect of nucleotide binding on the oligomerization state of MinD.

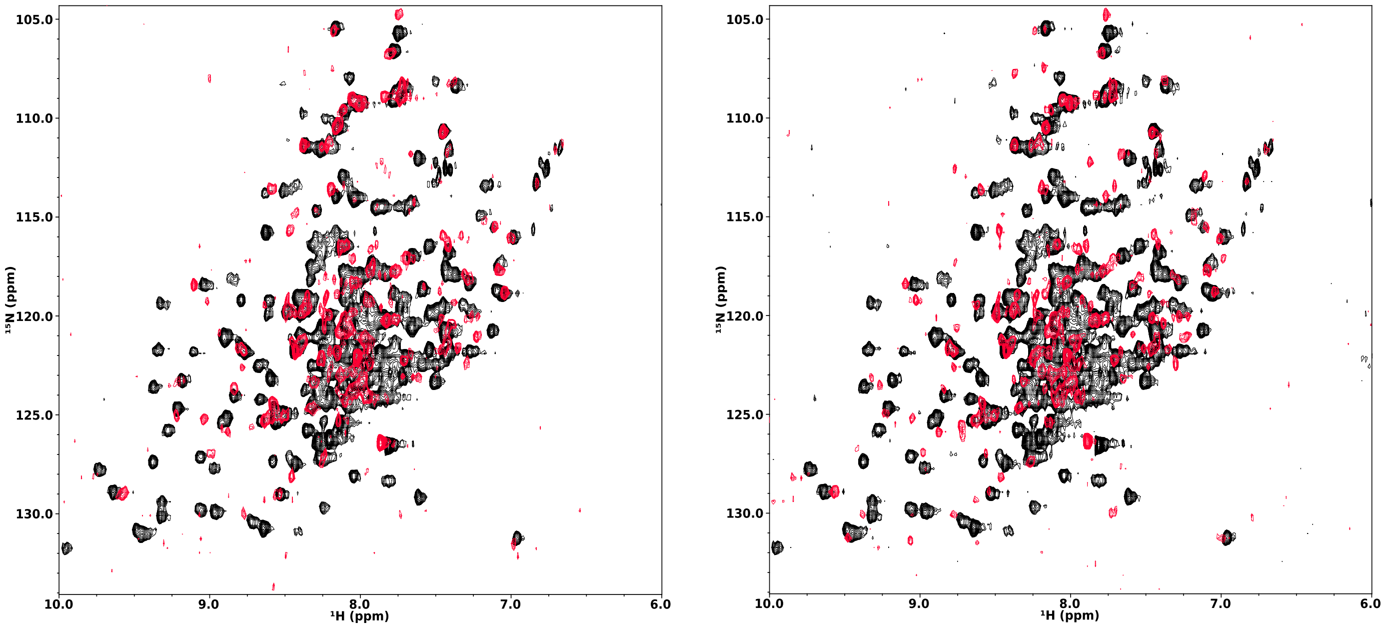

Figure 3.6 ^{1}H – ^{15}N HSQC of MinD D40A in the absence (black) and presence of 1mM ADP (red, left) or ATP (red, right) at 25°C, pH 7.2 with a MinD concentration of 50µM.

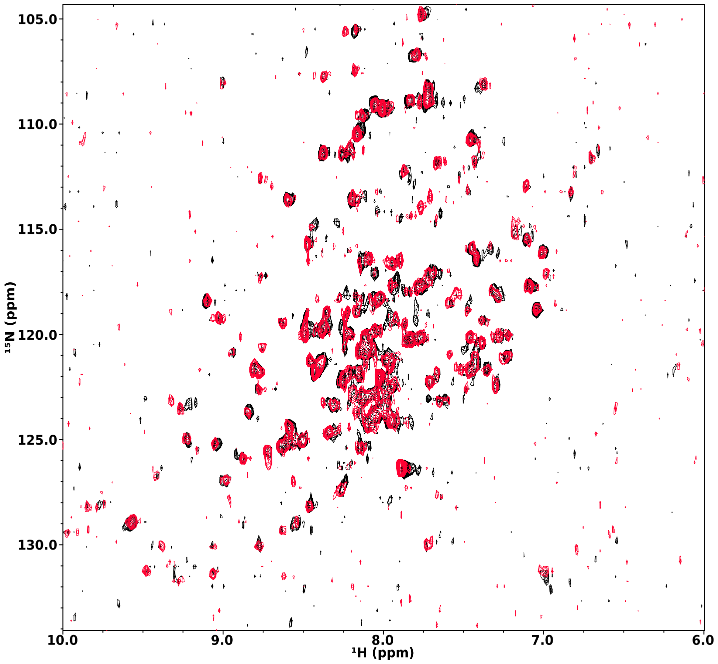

Figure 3.5 ^{1}H – ^{15}N HSQC of MinD D40A in the presence of 1mM ADP (black) or 1mM ATP (red) at 25°C, pH 7.2 with a MinD concentration of 50µM.

3.6 Investigation of MinD dimerization

To monitor changes in molecular weight induced by nucleotide binding, size exclusion chromatography was performed on MinD D40A in the presence of ADP or ATP. As shown in Figure 3.7, the elution profiles were virtually identical - both contained a single peak eluting at approximately 10.5mL, which corresponds to the expected elution volume for monomeric MinD. This suggests that there was no change in oligomerization state, demonstrating no dimer had formed by the binding of either nucleotide.

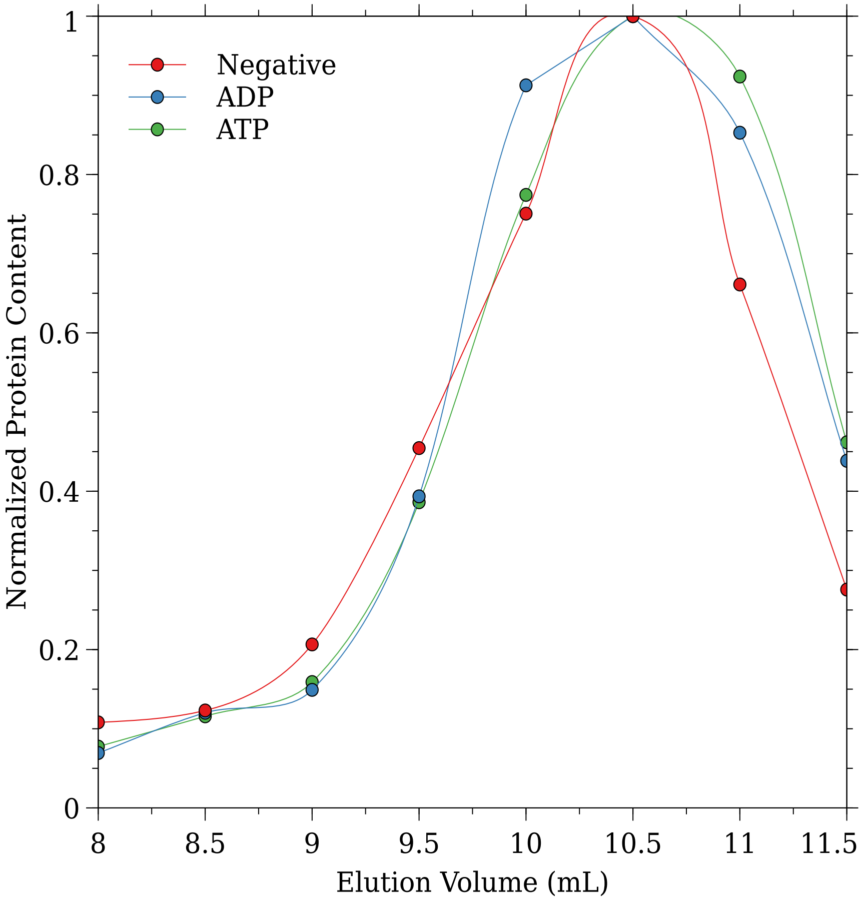

Figure 3.7 Size exclusion chromatography profile for MinD D40A. Samples were applied to a Superdex SP75 column in a buffer containing 5mM $MgCl_2$ and, where indicated, 1 mM ADP or ATP. Fractions were analyzed by Coomassie Blue-stained SDS-PAGE and protein amounts determined by ImageJ.

In order to test whether the D40A mutation is inhibiting dimer formation, the experiment was repeated with wild-type $MinD_{Ng}$. As shown in the elution profiles in Figure 3.8, a single peak eluting at the same volume was observed for the absence or presence of nucleotide, suggesting that wild-type $MinD_{Ng}$ also does not form a dimer. This experiment was performed in a range of buffer conditions (e.g. exchange buffer, NMR buffer, and PBS-T), but no change in elution volume was observed.

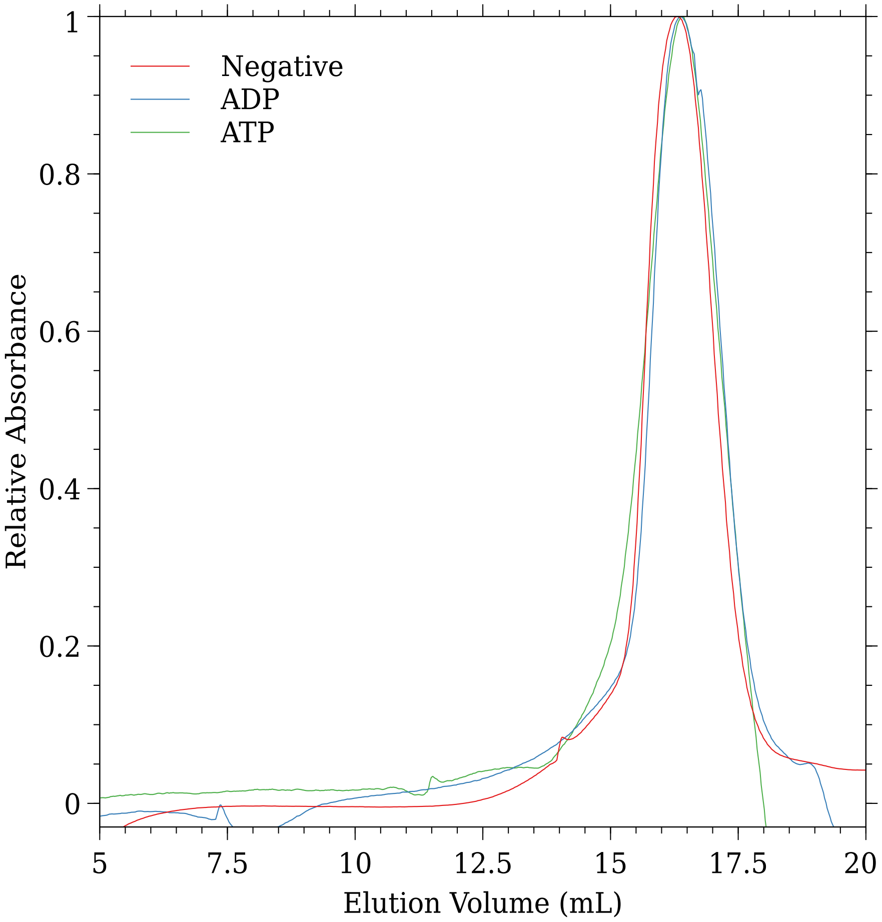

Figure 3.8 Size exclusion of wild-type MinD in the absence or presence of 1mM nucleotide. Samples were analyzed by FPLC using a Superdex SP200 column in a buffer containing 5mM $MgCl_2$ and 1mM nucleotide. Absorbance at 280nm was monitored.

3.7 Optimization of NMR conditions

While the spectrum of D40A MinD showed significant improvements over the spectrum of WT MinD, the quality of the spectrum was not appropriate for chemical shift assignment. To try and improve spectral quality, we were interested in running NMR experiments at higher temperatures, since this would increase molecular tumbling rates, which can improve peak resolution. To evaluate the stability of MinD D40A at higher temperatures, samples were incubated at various temperatures up to 37°C and solubility monitored by SDS-PAGE of the soluble fractions. As shown in Figure 3.9, sample solubility was adversely affected by increasing temperature with loss of 50% of the sample after only 1 day at 37°C.

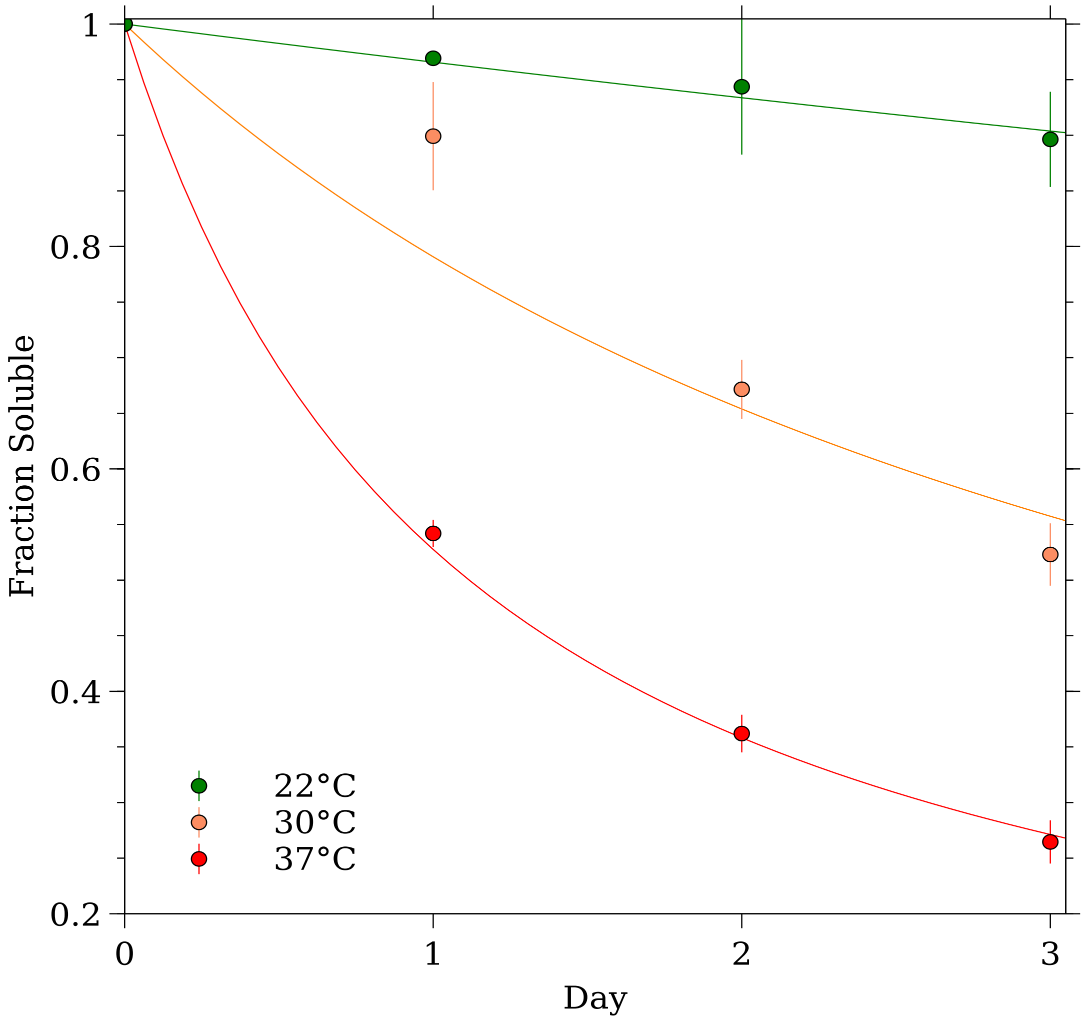

Figure 3.9 Temperature dependence of MinD D40A stability. 30 µuM MinD D40A was incubated in a buffer comprised of 50 mM Tris pH 8.5, 100 mM NaCl, and 0.2 mM EDTA. Aliquots were removed at various time points and the soluble fraction analyzed by Coomassie Blue-stained SDS-PAGE. Protein content in each aliquot was estimated by integrating gel band intensity with ImageJ.

We also tested the stability of MinD at a pH that is closer to neutrality, since this can improve the sensitivity of amide proton-detected NMR experiments. For this purpose, $^{1}H - {}^{15}N$ HSQC spectra were acquired on a sample of MinD D40A in a buffer at a pH 7.2 at regular intervals, and the volume of a selected reporter peak measured at each time point. As shown in Figure 3.10, a significant decrease in peak volume was observed over time. As peak volume reports on the abundance of the soluble population, this suggests that solubility was adversely affected by bringing the pH down to 7.2.

Taken together, these results indicate that MinD D40A, despite improved spectral quality over the wild-type protein, was still not a reasonable candidate for high-resolution triple resonance experiments required for chemical shift assignment.

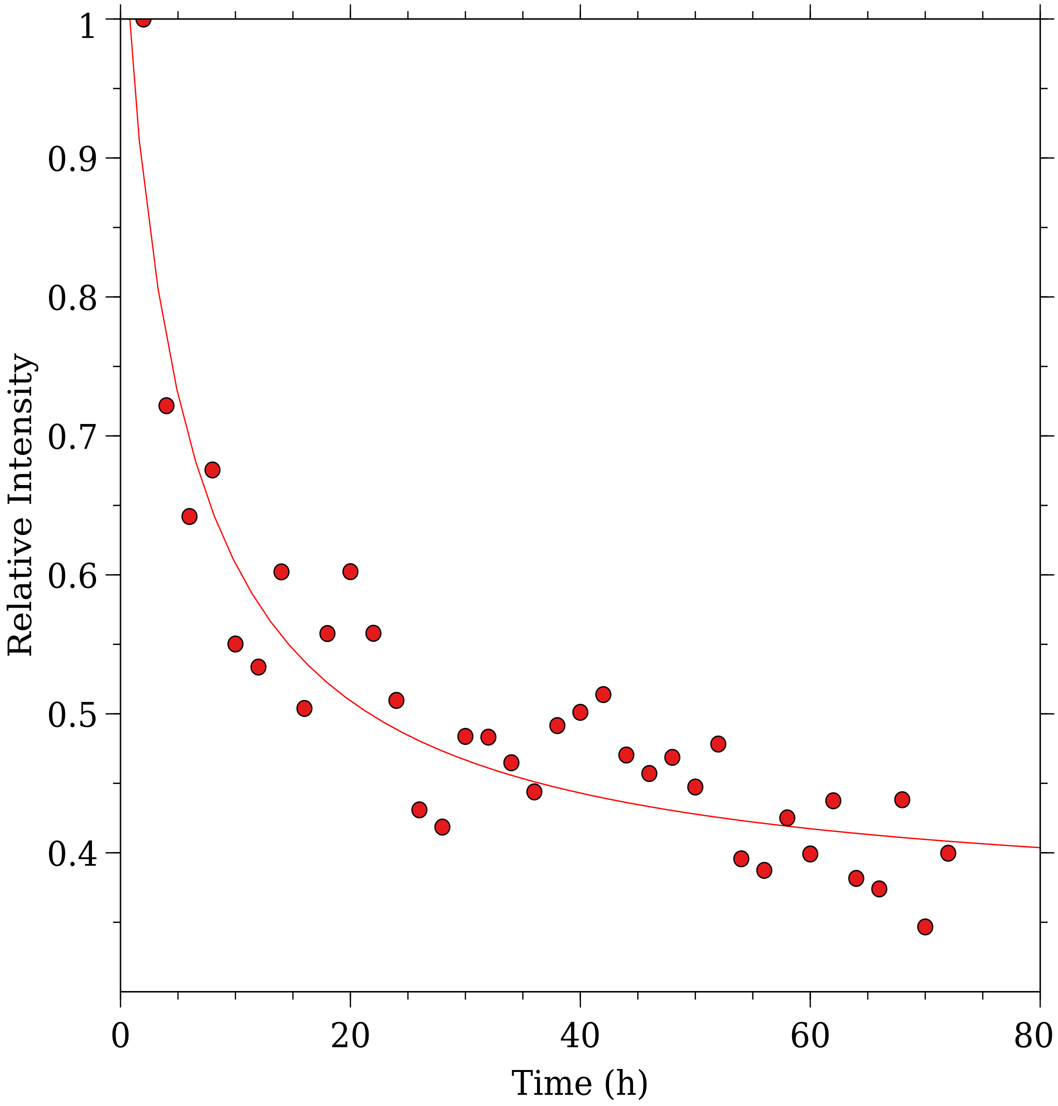

Figure 3.10 Stability of MinD D40A in solution at neutral pH. $^{1}H - ^{15}N$ HSQC spectra were collected hourly of uniformly ^{15}N-labelled MinD D40A at 25°C, pH 7.2 with a MinD concentration of 50µM. One distinct, well-resolved peak was selected to be integrated every hour using NMRPipe.

3.8 Overexpression and purification of MinD ΔC10

In an attempt to further increase the solubility of a MinD sample for solution NMR studies, a truncation mutant of MinD missing the last 10 residues that form a membrane-binding amphipathic helix was made (MinD ΔC10). As shown in Figure 3.11, protein yields were significantly improved over both WT an D40A

MinD, with higher concentrations of MinD being isolated at the end of the purification. However, in this final sample two species were detected; one at the expected molecular weight for MinD ΔC10 (~30 kDa) and another at approximately twice this molecular weight.

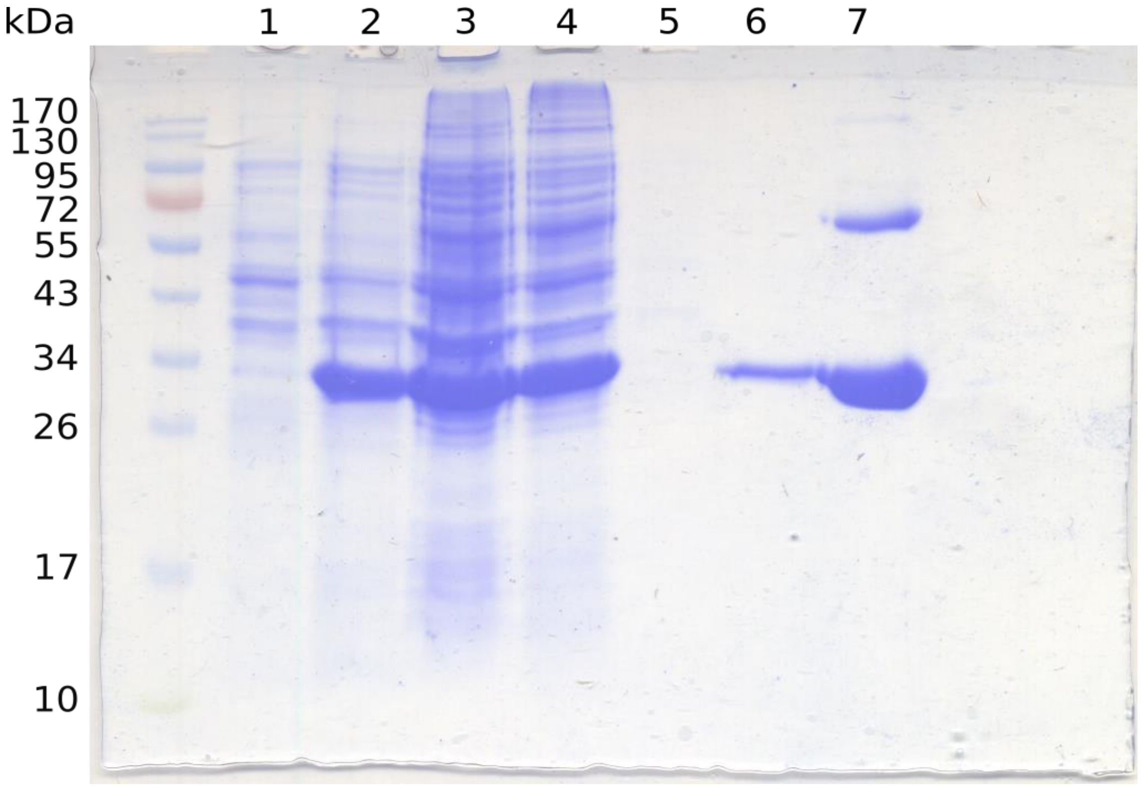

Figure 3.11 Purification of MinD ΔC10. Samples were taken of 1) cell culture before; and, 2) after induction of expression; 3) whole-cell lysate; 4) the soluble fraction of the lysate; 5) nickel column flow-through; 6) low imidazole nickel column wash; 7) nickel column elution.

3.9 Identification of a covalently linked MinD dimer

Additional evidence that MinD ΔC10 forms a dimer was provided by size exclusion chromatography profiles obtained during purification. As shown in the UV traces (Figure 3.12), a peak eluted at 9mL in addition to the peak corresponding to the monomeric state at 11mL. This peak was intermittently observed during purifications of all three constructs used in this study. Deconvolution of the UV trace suggested that there were two additional species in this elution profile, with one being a very high molecular weight aggregate of MinD, and then the species that elutes at 9mL. To determine the molecular weight of this species, MALS was performed in tandem with size exclusion chromatography. This experiment showed that the molecular mass of the peak at 9 mL was ~62 kDa, which is approximately twice the mass of the peak that eluted at 9 mL (MALS calculated mass of 29 kDa), suggesting the presence of a dimeric state.

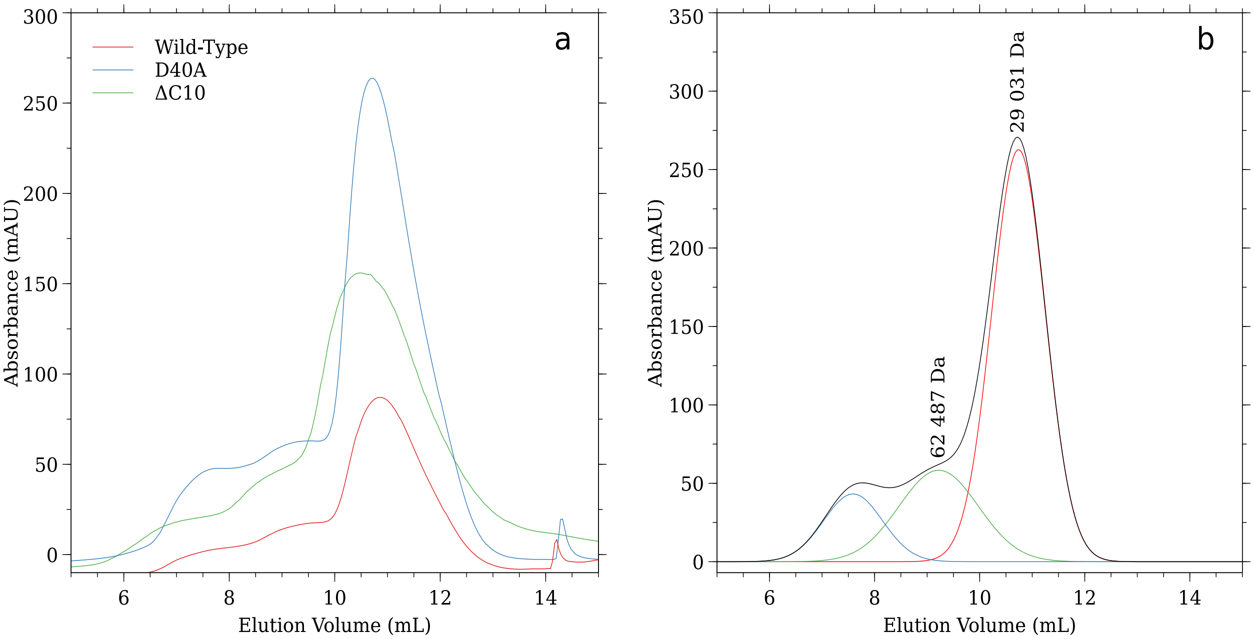

Figure 3.12 UV traces of MinD constructs analyzed by size exclusion chromatography. A) Sample spectra collected of all three constructs used; b) Spectral deconvolution of the UV trace from MinD D40A (black) with molecular weights of each component peak (coloured) indicated. Samples were analyzed by FPLC on a Superdex SP75 column, with absorbance at 280nm monitored. Molecular weights were estimated using MALS. Deconvolution was performed by fitting Gaussian peaks using Fityk.

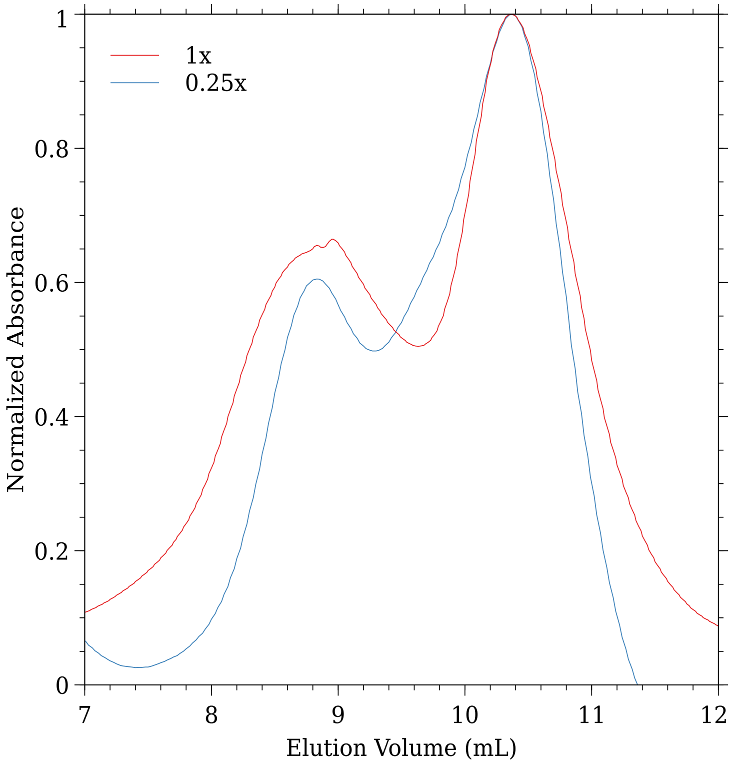

Figure 3.13 Normalized UV traces from size exclusion chromatography with samples of MinD ΔC10 immediately after purification (red), and after diluting 4-fold (blue).

Observation of a dimeric state for ΔC10 in the absence of added nucleotide was surprising, especially since dimerization was not observed for full-length MinD, even in the presence of ATP. To determine if this was a reversible concentration-dependent interaction, purified samples were diluted and reanalyzed by size exclusion chromatography. As seen in Figure 3.13, there was a slight decrease in the relative population of dimer, although it was not eliminated.

The poor reversibility of the dimer, and its resistance to disruption by SDS-PAGE suggested that the dimer was the result of a covalent link between two surface-exposed cysteine residues. This was confirmed by exposing the sample to a reducing agent during size exclusion chromatography, which eliminated observation of the dimeric species in the elution profile (Figure 3.14).

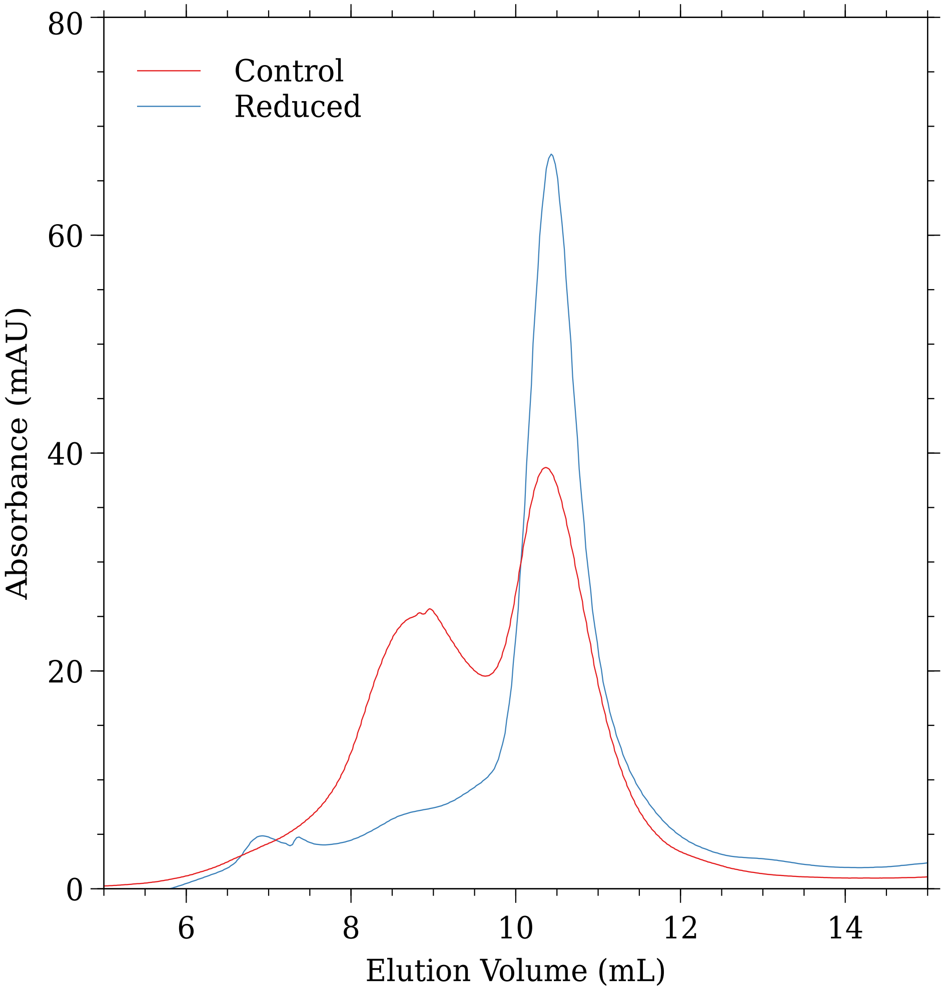

Figure 3.14 UV traces from size exclusion chromatography performed on MinD ΔC10 in the absence or presence of 5% 2-mercaptoethanol.

The discovery of a covalently linked dimer species raised the possibility that the purified protein had mis-folded. To assess the secondary structure content, circular dichroism spectra of MinD ΔC10 in the absence and presence of reducing agent were collected. As seen in Figure 3.15 the CD spectra overlap extensively, suggesting that the presence of a disulfide bond has not impacted secondary structure.

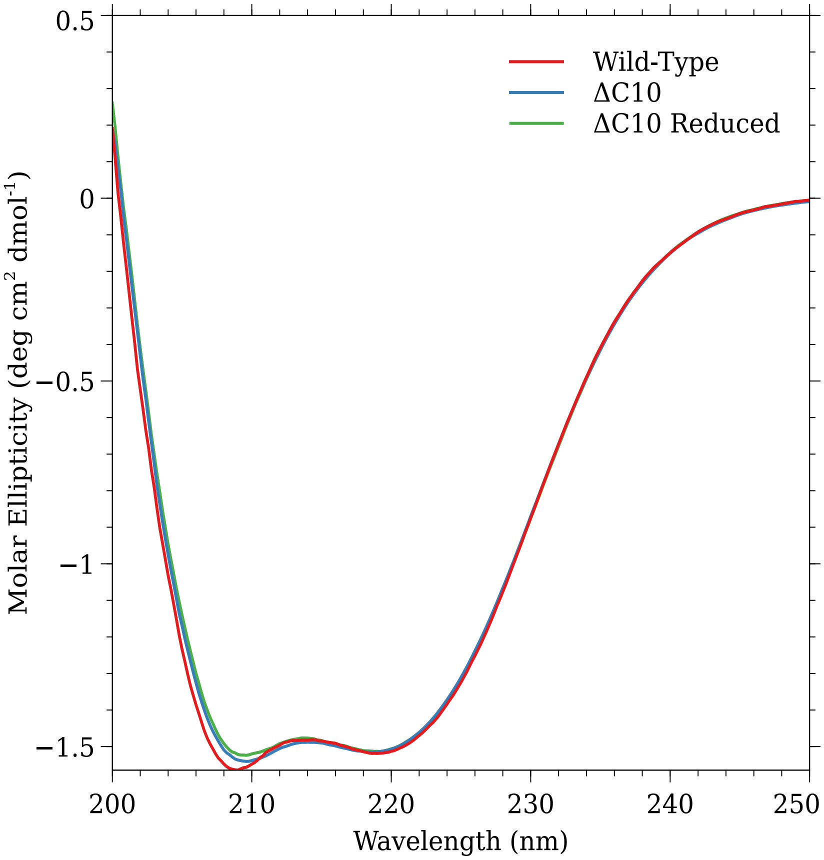

Figure 3.15 CD spectra of MinD in reducing conditions. Samples contained 10µM MinD at 25°C, pH 8.5. Reduced sample was incubated with 1mM TCEP prior to analysis.

3.10 Backbone Assignment of MinD ΔC10

Given the high solubility of MinD ΔC10 and ability to preserve the monomeric state through the use of reducing agents, we decided to use this sample to assign backbone chemical shifts. However, in the suite of triple resonance experiments that were run for this purpose (HNCO, HNCA, and CBCA(CO)NH spectra), very few correlations were observed (Figure 3.16), likely due to the large size of MinD (~30 kDa). For this reason, it was necessary to include deuteration in the sample labeling scheme, since the smaller gyromagnetic ratio of this nucleus greatly reduces the dipole interaction with other nuclei that can reduce resolution and sensitivity. For this purpose, *E. coli* expressing MinD ΔC10 was cultured in a D_2O-based media using standard protocols (77).

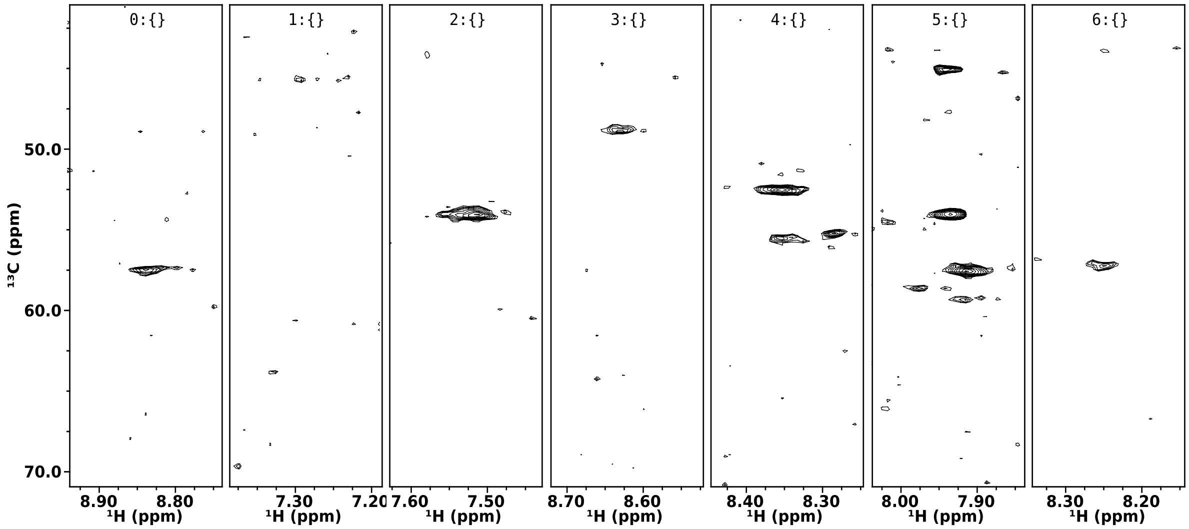

Figure 3.16 Sample strip plots of the HNCA spectrum recorded for MinD ΔC10. Some strips contained 2 peaks as expected (strips 4, 5 and 6), or were missing an inter-residue correlation (strips 0, 2, and 3), or had zero peaks (strip 1).

Since protein yields are typically reduced when expression is done in D_2O, various conditions were tested to identify the best protocol to produce deuterated MinD ΔC10. As shown in Figure 3.17, when cells were first cultured in LB media before transfer into deuterated minimal media, a high level of MinD expression was induced prior to addition of IPTG. Although this gave rise to protein expression levels that were comparable to those obtained for using the H_2O-based media in the final expression culture, the high level of expression that was obtained prior to transfer into D_2O expression media would reduce the proportion of deuterated sample. In contrast, if an LB pre-culture was first transferred to an H_2O-based media and allowed to reach mid-log phase before being transferred into deuterated media, then expression was only observed in the deuterated culture. Even though there is a ~40% decrease in expression relative to the previous expression trials, this scheme would give rise to the largest proportion of deuterated protein. Therefore this scheme was chosen to make a ^2H, ^{13}C, ^{15}N-labeled MinD ΔC10 sample for triple-resonance NMR experiments. As shown in Figure 3.18, the ^1H – ^{13}C HSQC spectrum of the deuterated sample compared to that from the protonated sample showed very few peaks, signifying a level of deuteration consistent with the >90% deuteration that is usually obtained for these samples (77). Most importantly, almost no signal intensity was retained at the CA position, which will give rise to significant reduction of transverse relaxation, leading to greater resolution and sensitivity.

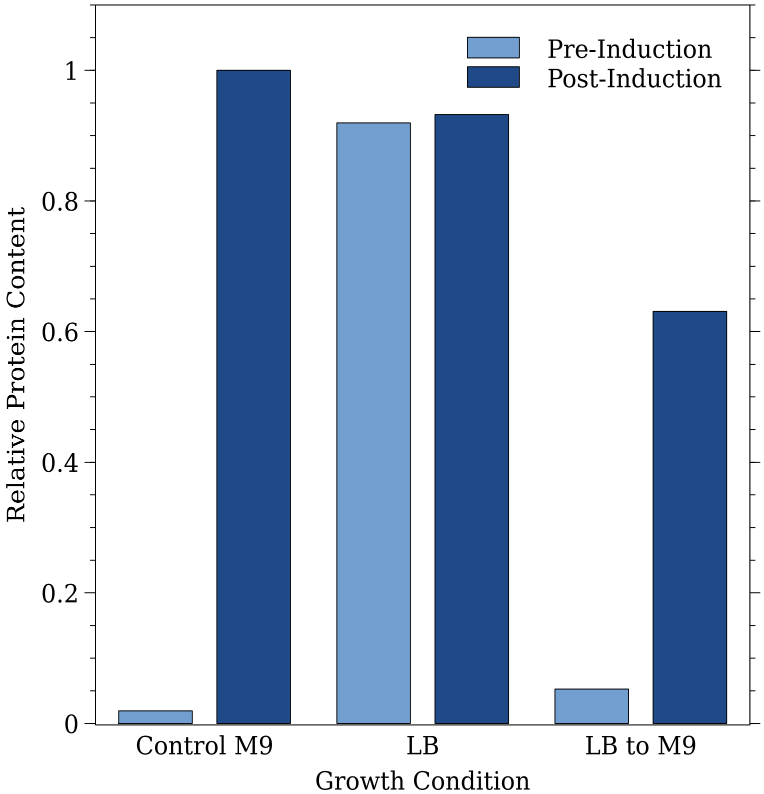

Figure 3.17 Relative expression of MinD ΔC10 under various deuteration schemes. Samples of culture were taken before the addition, and 18 hours after the addition, of 0.5mM IPTG, then run on a 12% acrylamide gel and stained with Coomassie Blue. Protein content in each sample was estimated by integrating gel bands with ImageJ.

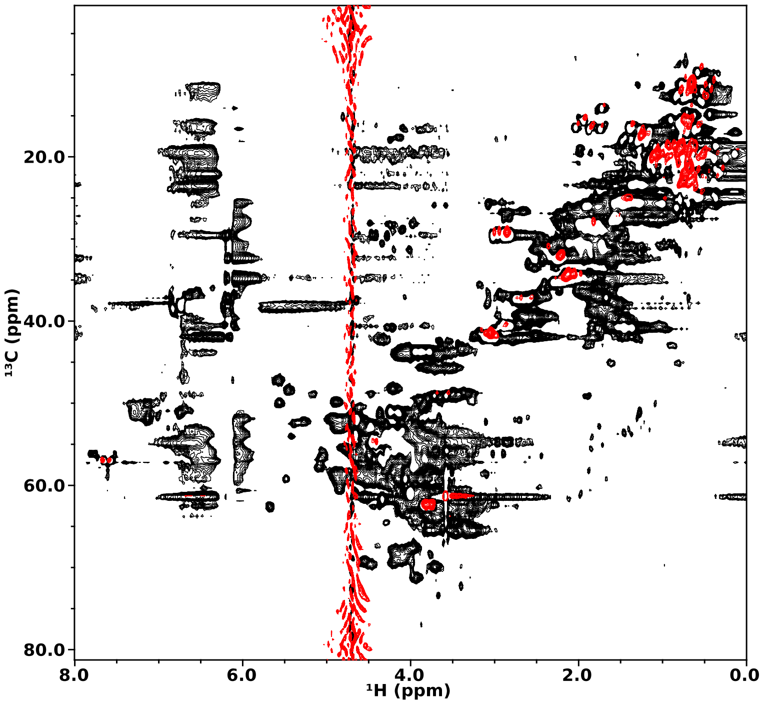

Figure 3.18 ^{1}H – ^{13}C HSQC of uniformly ^{13}C,^{15}N-labelled MinD ΔC10 without (black) and with (red) deuteration at 25°C, pH 7.2 with a MinD concentration of 350μM.

Triple resonance experiments for backbone assignments that were performed on the deuterated sample include the TROSY HNCA, HN(CO)CA, HN(CA)CB, HN(COCA)CB, HNCO, HN(CA)CO. While the quality of these spectra was markedly improved over those acquired on the protonated sample, there were still a significant number of missing correlations that made it impossible to uniquely map linked chemical shifts to the protein primary sequence. An example of this is shown in Figure 3.19, where linkages to the i+1 residue could be identified but no correlations to the preceding residue were observed.

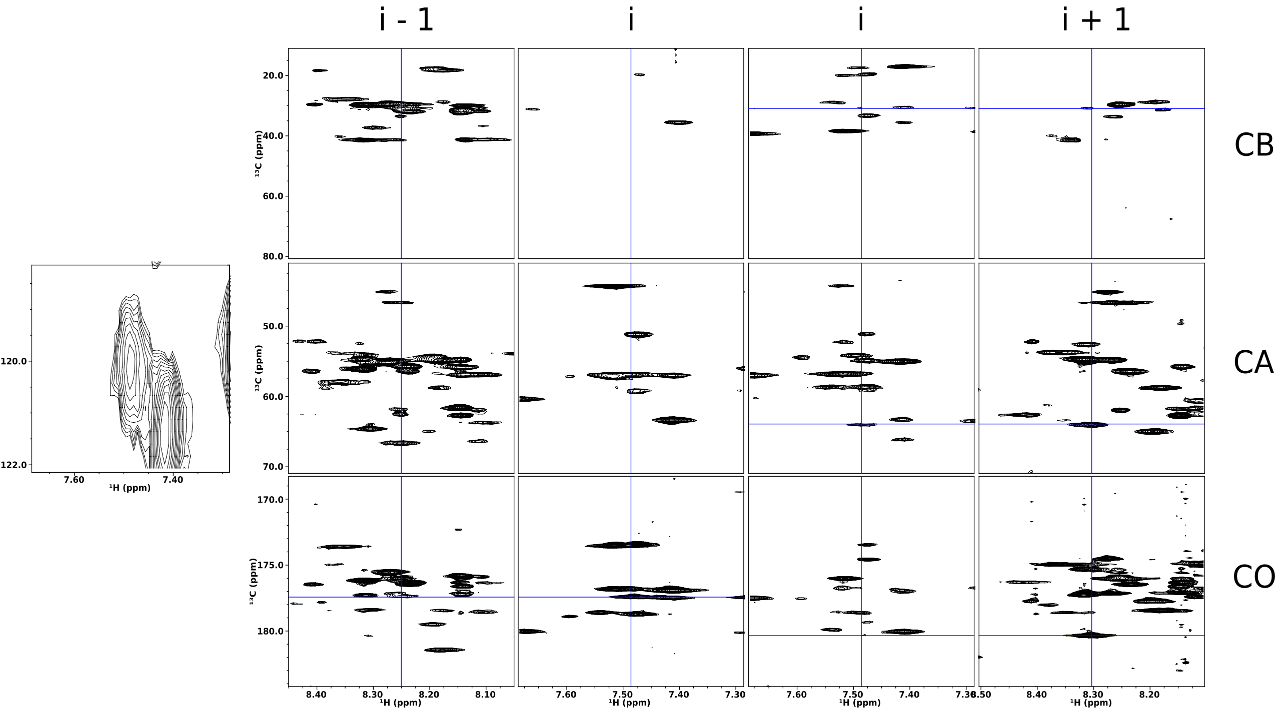

Figure 3.19 Example of a residue that showed incomplete correlations in backbone assignment spectra. Each strip should contain a peak on the center line (blue vertical line), at a vertical position which aligns with the neighboring strip (blue horizontal line). Only two linkages are apparent, between the i and i+1 CA positions, and the i and i-1 CO positions. The reference HNCO peak is displayed left.

To help reduce the number of ambiguities in chemical shift assignment, selective labeling was investigated to help identify peaks arising from specific amino acids. Usually this is done by expressing unlabeled protein with the incorporation of selectively ^{15}N-labelled amino acid. However, a more cost-effective way to obtain the same information can be done to selectively introduce unlabeled (^{14}N) amino acids into ^{15}N-labeled growth media, resulting in the elimination of peaks of that amino acid type (78). This selective unlabeling was performed for the most abundant amino acids in MinD, being lysine (16 total), arginine (15 total), and isoleucine/leucine/valine (60 combined), with their corresponding spectra being displayed in Figure 3.20. Peaks that were reduced in intensity or disappeared indicated positions that had been unlabeled. While there was some overlap with unlabeled peaks, enough positions were uniquely unlabeled to assign residue type with a high level of confidence.

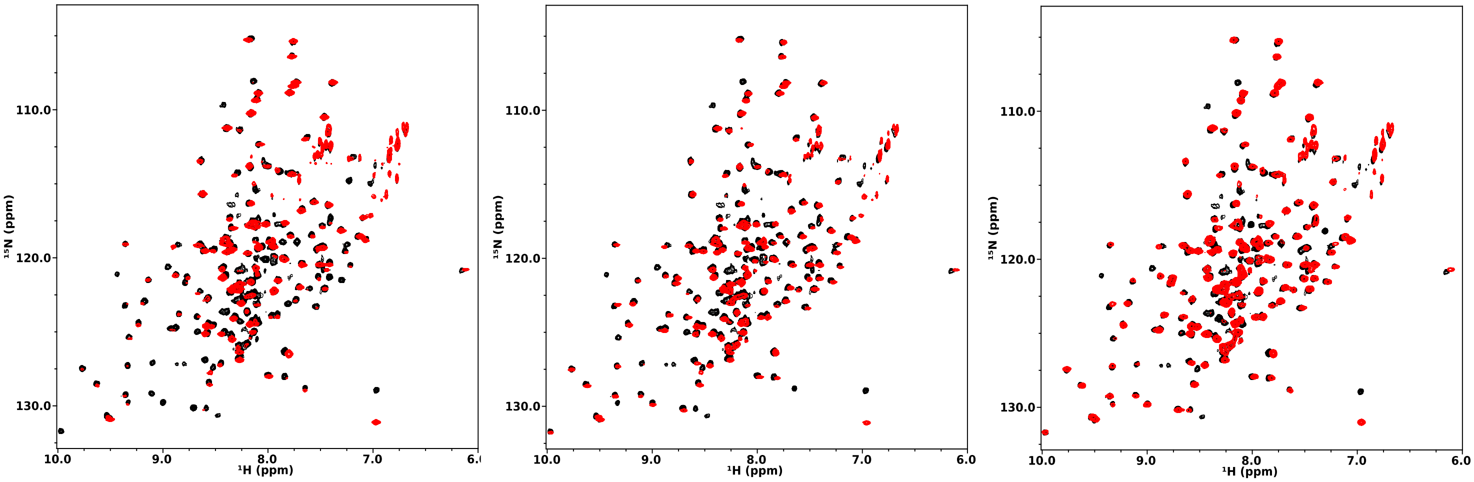

Figure 3.20 ^{1}H – ^{15}N TROSY of selectively unlabeled samples. Uniformly ^{15}N-labelled (black), ^{14}N-unlabelled Ile/Leu/Val (red, left), ^{14}N-unlabelled Lys (red, center), and ^{14}N-unlabelled Arg (red, right) MinD ΔC10.

This information was used in conjunction with the linkages attained from the triple resonance experiments, making it possible to assign 93 % of the peaks arising from backbone amide protons in the ^{1}H-^{15}N TROSY spectrum of MinD ΔC10, shown in Figure 3.21. This gave rise to partial assignment of backbone atom chemical shifts for 200 of the 263 non-proline MinD ΔC10 residues (76% of the expected peaks).

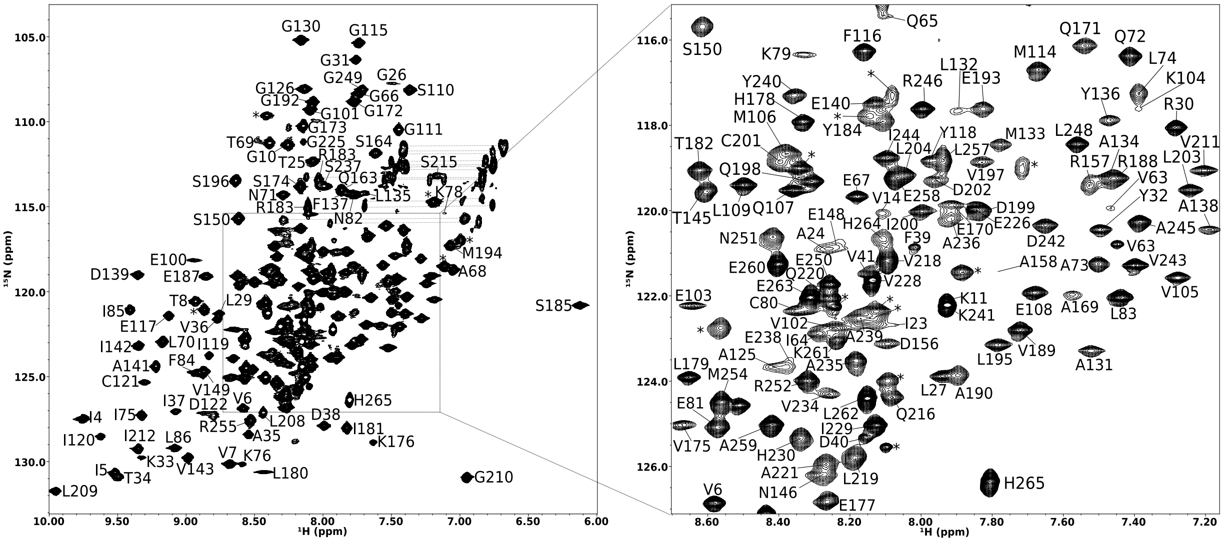

Figure 3.21 Assigned ^{1}H – ^{15}N TROSY spectrum of MinD ΔC10. Triple resonance experiments were carried out on a sample of uniformly 13C,15N-labelled protein with sidechains deuterated at 25°C, pH 7.2 with a MinD concentration of 1.4mM. Asterisks indicate unassigned residues; dotted lines indicate amide side chain peaks.

3.11 Estimation of MinD secondary structure

While several crystal structures of $\mathrm{MinD_{Ec}}$ have been captured, none are available for $\mathrm{MinD_{Ng}}$. Therefore a homology structure was generated for $\mathrm{MinD_{Ng}}$ using the SWISS-MODEL server (79). The template chosen was the structure of dimeric $\mathrm{MinD_{Ec}}$ D40A ΔC10 bound to $\mathrm{Mg^{2+}}$ and ATP (PDB 3Q9L). This gave rise to a model of good quality (QMEAN score of -0.36) (80), as shown in Figure 3.22. As expected, given the high level of sequence identity between the two proteins, the homology structure was highly similar to that of the template, with the main difference being in the length and positions of unstructured loops between secondary structure elements.

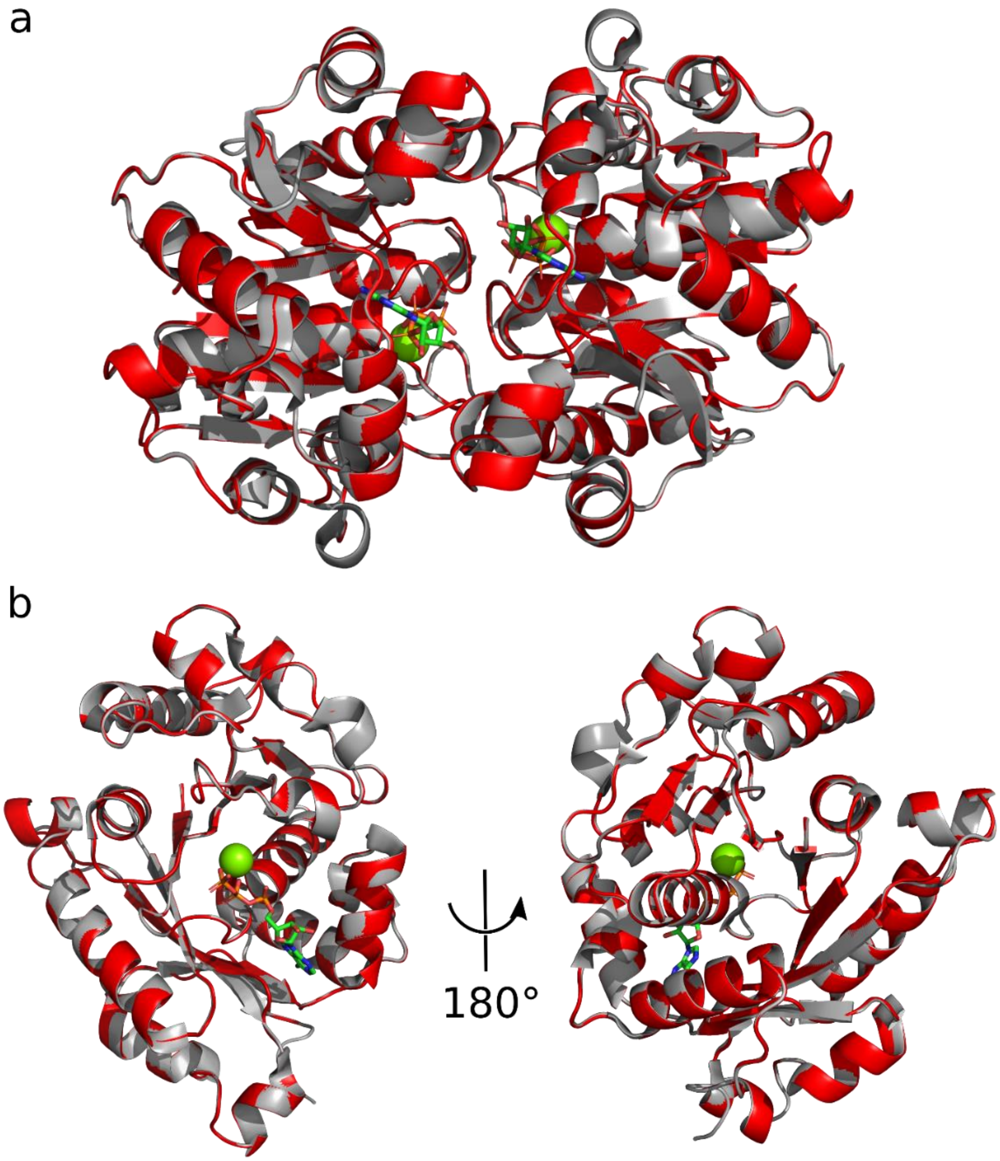

Figure 3.22 Predicted structure of $\mathrm{MinD_{Ng}}$. Using the SWISS-MODEL server, a homology model of $\mathrm{MinD_{Ng}}$ (red) was generated using ATP-bound $\mathrm{MinD_{Ec}}$ (grey) as a template. Shown are cartoons of both the nucleotide-bound dimer (a) and an individual subunit (b). Bound magnesium is shown as a ball and a stick representation of ADP is shown.

The assigned residues were mapped onto the homology model in Figure 3.23, and showed that most of the assigned residues are on the side of the protein that is not involved in nucleotide binding or dimerization. Secondary chemical shifts were calculated to identify secondary structure elements (Figure 3.24), and showed good agreement with the homology model, except for residues 215-230 which appear to be β-structured in MinD ΔC10.

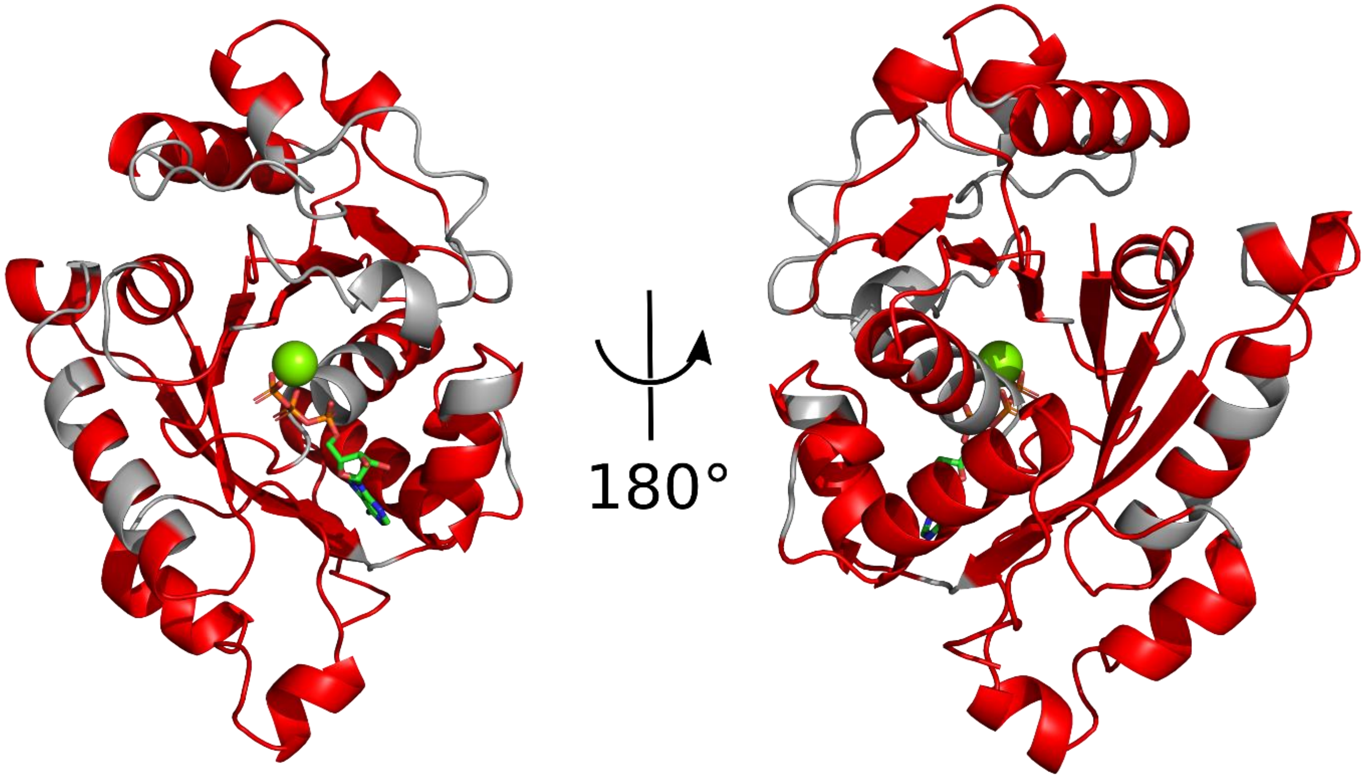

Figure 3.23 Residues assigned through triple resonance experiments mapped onto the homology structure of MinD$_{Ng}$. Assigned positions are shown as red, unassigned positions are grey.

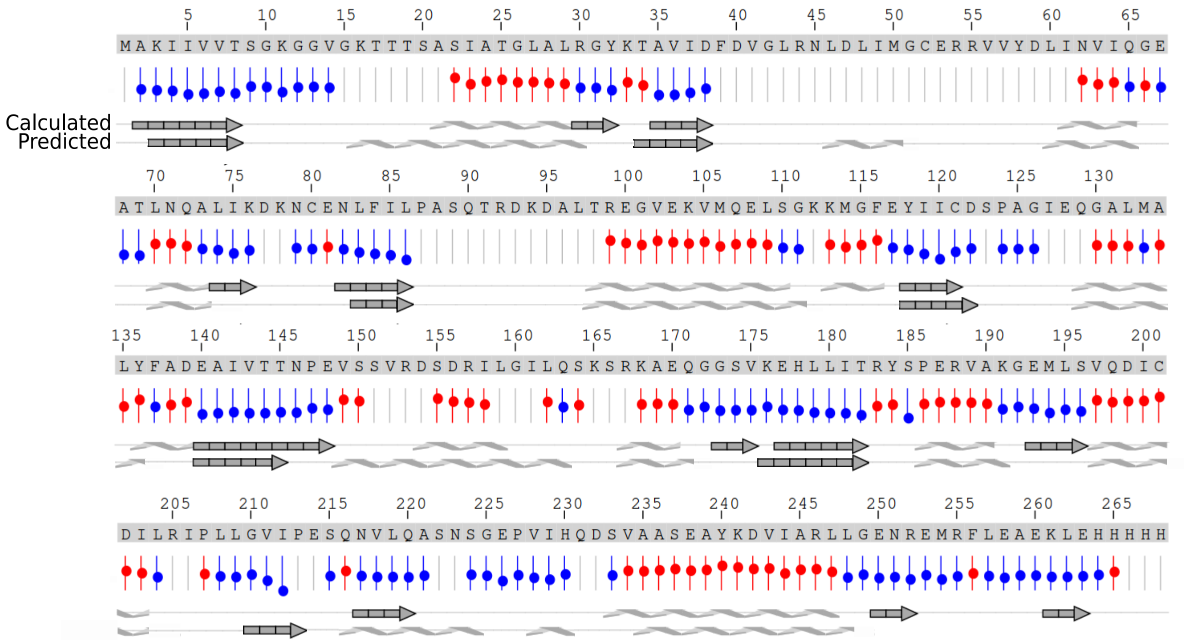

Figure 3.24 Secondary structure content of MinD$_{Ng}$. Content was determined by Cα secondary shift calculations (calculated) and predicted from the homology model (predicted). Arrows represent beta strands (blue secondary shifts), coils represent helices (red secondary shifts). The magnitude of the secondary shift value is indicated by the vertical position of the red or blue balls for each residue.

3.12 Measurement of nucleotide binding affinities

In order to measure the affinity of nucleotide binding to MinD ΔC10, four well-resolved peaks where chosen to be reporters of nucleotide binding (Figure 3.26), and peak volumes were quantitated as a function of nucleotide concentration. These peaks represent residues distributed throughout the structure of the protein (Figure 3.25), and decrease in intensity as nucleotide concentration increases, with a new peak appearing at a different position and concomitantly increasing in intensity. These were used to measure the relative population of bound and free protein as a function of nucleotide concentration (Figure 3.27), and gave rise to indistinguishable dissociation constants for ATP and ADP, with a value of 250µM.

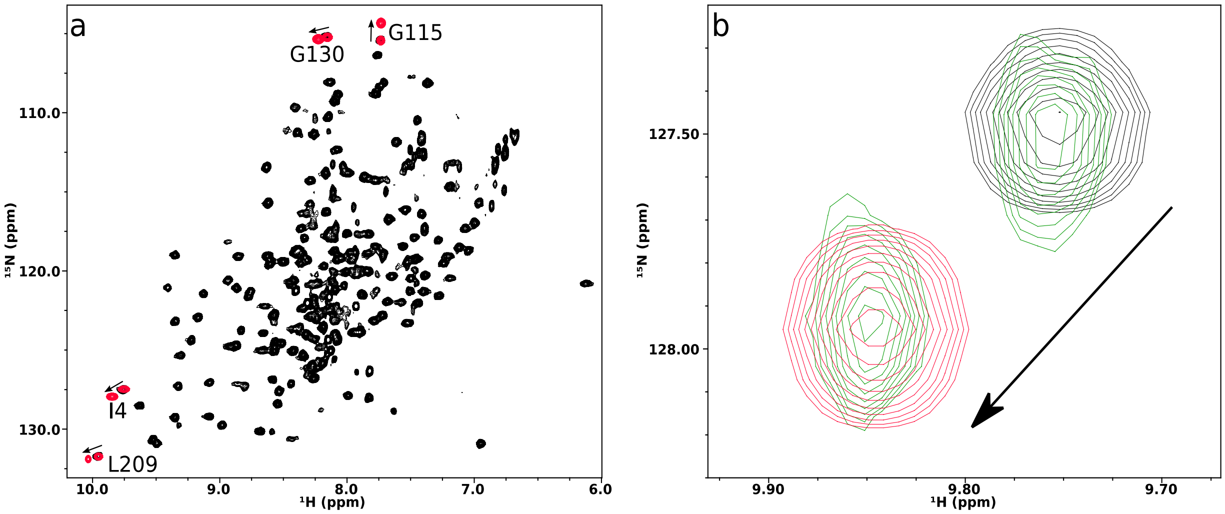

Figure 3.26 Selection of reporter peaks for nucleotide binding. a) ^{1}H – ^{15}N TROSY of MinD ΔC10 (black). Four well-resolved peaks were selected and integrated to act as reporters of nucleotide binding (shown in red, labeled). b) Amide peak of I4 in the absence of ATP (black), in the presence of a half-saturating concentration of ATP (green), and fully bound (red). Arrows indicate movement of peaks upon binding.

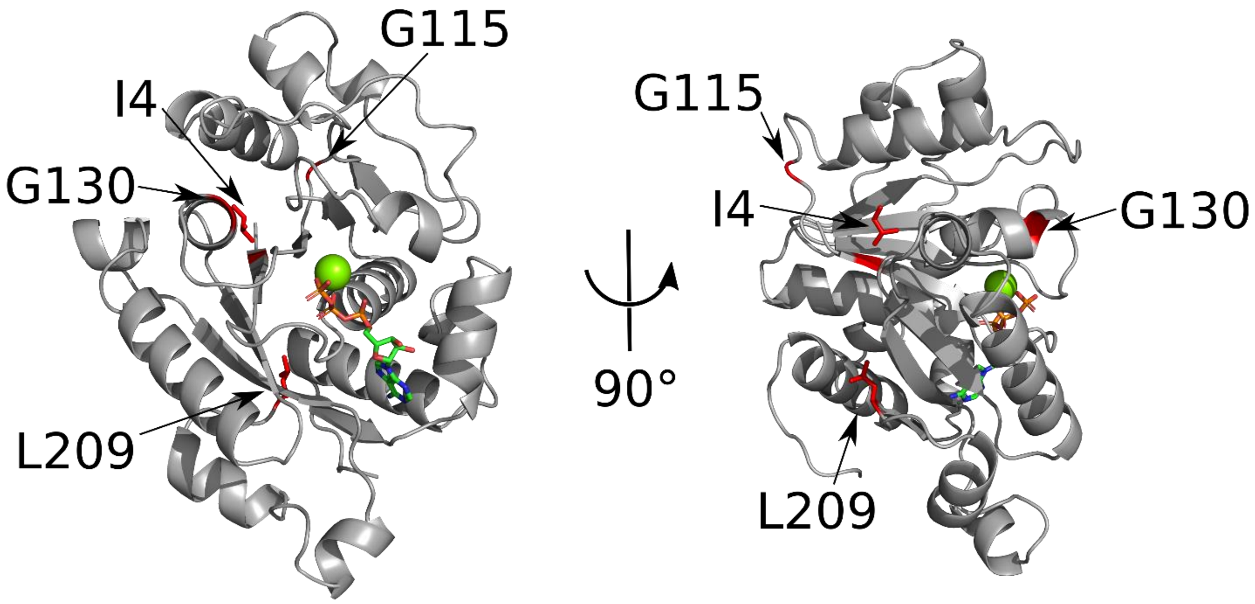

Figure 3.25 Location of nucleotide binding reporter peaks on the homology model of MinD$_{Ng}$. Reporter peaks are labeled, shown red with sidechains drawn.

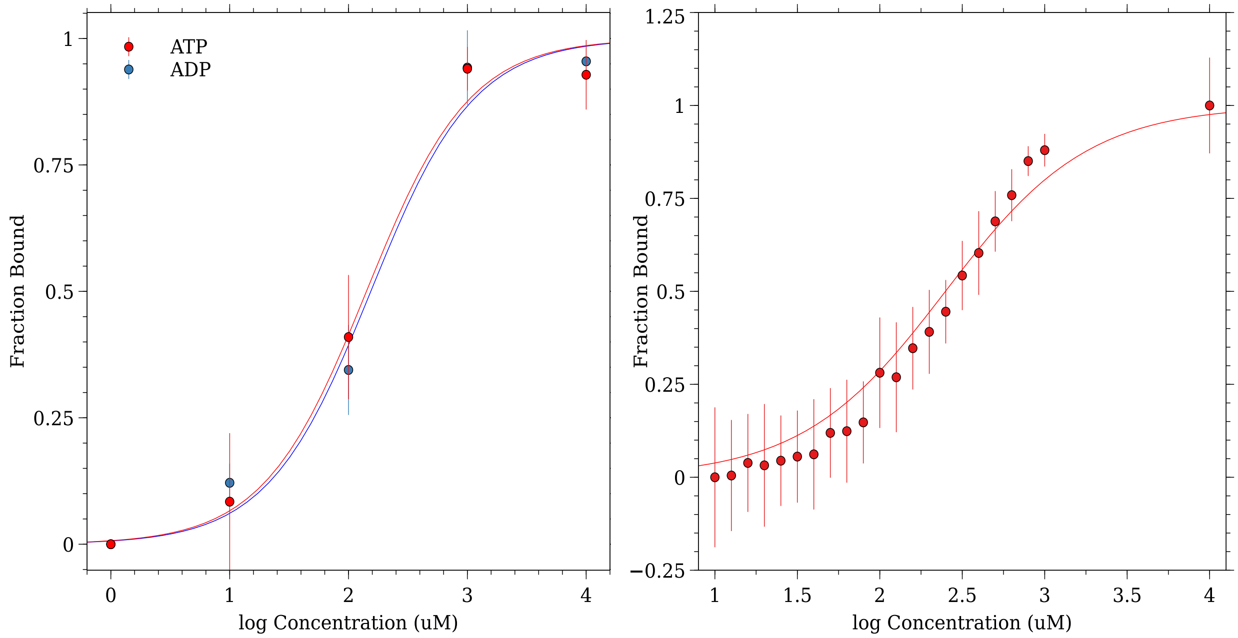

Figure 3.27 Titration of MinD ΔC10 with ADP and ATP. The fraction of a population of MinD ΔC10 bound in the presence of increasing ADP or ATP (left), and in the presence of increasing ATP with more frequent sampling (right) are shown. Shown binding curves are fit with Kd of 250µM. Samples contained 150µM (left) or 800µM (right) MinD ΔC10. A ^{1}H – ^{15}N TROSY was recorded at each total nucleotide concentration, from which four reporter peaks were selected and integrated using NMRPipe. Poor spectral quality prevented determination of free nucleotide concentration.

4 Discussion

4.1 MinD$_{Ng}$ forms a non-physiological dimer

Our observation that MinD$_{Ng}$ can form a dimer in the absence of ATP was surprising in light of all the evidence for ATP-dependent dimerization in MinD$_{Ec}$. However, the dimer observed in our experiments was mediated by an inter-molecular disulfide bond which would not be expected to form in the reducing environment of the bacterial cytoplasm. It is therefore likely that disulfide formation is an artifact of the purification process, and not inherent to the protein itself. This can be easily avoided by purifying under reducing conditions.

Circular dichroism and solution NMR analysis of MinD$_{Ng}$ in reducing conditions did not demonstrate any change in secondary structure, suggesting that disulfide bonds are formed by surface-accessible Cys residues. The residues responsible for disulfide bond formation are not known, with three Cys residues that could be considered to be reasonably accessible on the protein surface. Two of the four Cys in MinD$_{Ng}$ are conserved in MinD$_{Ec}$ – as disulfide formation has not been reported for MinD$_{Ec}$ it is therefore probable that one or both non-conserved Cys are involved in disulfide bond formation. Of these residues, the sidechain of C201 is the most surface accessible, but its presence in a helix does not allow a great deal of conformational mobility. The accessibility of C201 in the native conformation makes it the most likely candidate for disulfide formation. It remains possible that C201 from one subunit bonds with C80 of another subunit, although this should give rise to higher order oligomers which have not been seen.

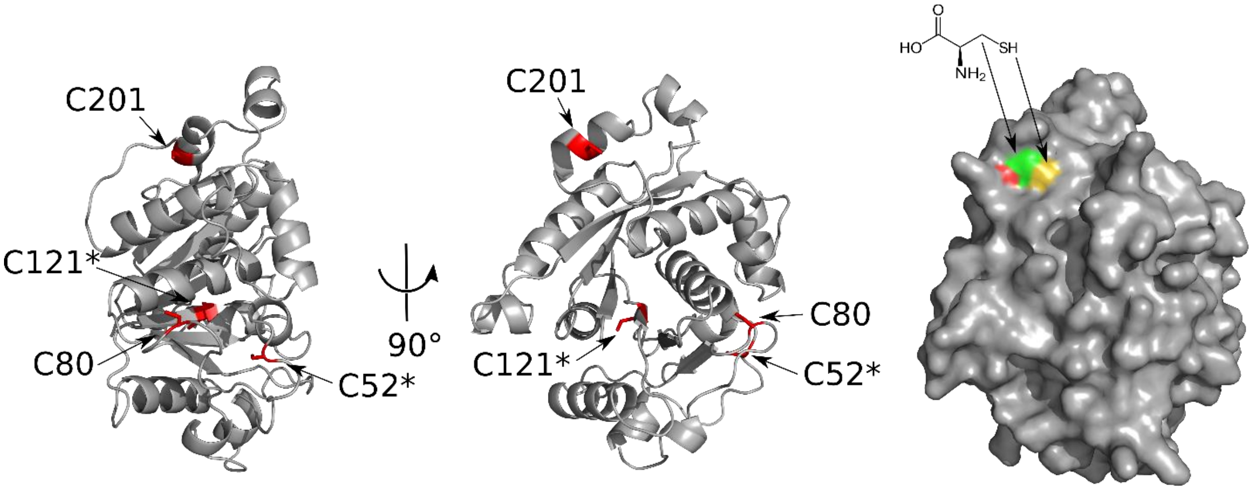

Figure 4.1 Location of Cys residues in the MinD$_{Ng}$ homology structure. Cys residues are coloured red with side chains drawn. Asterisks indicate residues conserved in MinD$_{Ec}$. Location of the sulfur atom of C201 is shown in yellow on the surface representation (right).

Although there are no reports of disulfide bond formation in $\mathrm{MinD_{Ec}}$ this may simply be a result of the different purification processes used for these homologues. Specifically, $\mathrm{MinD_{Ec}}$ purification is normally carried out by ion-exchange chromatography (35, 81), whereas we are using nickel affinity chromatography to purify $\mathrm{MinD_{Ng}}$. It is possible that the dimeric, disulfide-bound species elutes at a different ionic strength than the monomer, allowing pure monomeric $\mathrm{MinD_{Ec}}$ to be isolated. While it may be possible that a disulfide bonded $\mathrm{MinD_{Ec}}$ dimer could be detected by SDS-PAGE under non-reducing conditions, no such experiment has been reported, making it impossible to rule out.

One possibility that remains to be explored is that the C-terminal hexahistidine tag that is included in the $\mathrm{MinD_{Ng}}$ construct used in our studies may be facilitating this non-native disulfide-bond formation. However, the C-terminus of $\mathrm{MinD_{Ec}}$ is unstructured in crystal structures, suggesting that the addition of a tag at this site should have minimal impact. Indeed, ATP hydrolysis is observed for this construct at rates that are similar to those measured for the tag-free $\mathrm{MinD_{Ec}}$, supporting a wild-type fold for the hexahistadine-tagged protein. In addition, no disulfide-bonded dimers have been reported for a $\mathrm{MinD_{Ec}}$-hexahistadine fusion protein, casting further doubt that the histadine tag is responsible (37).

Conflicting studies of dimerization of $\mathrm{MinD_{Ng}}$ suggest that ATP promotes dimerization to a lesser extent than seen in $\mathrm{MinD_{Ec}}$ (27), while an earlier study reports that $\mathrm{MinD_{Ng}}$ purifies as a dimer (16). In the partial dimerization condition, a persistent population of dimer was observed even in the absence of nucleotide. Both studies can be explained by the identification of this non-physiological dimer. The persistent population of dimer was likely due to disulfide formation, similar to observations from purification of MinD ΔC10. The conclusion that ATP was inducing dimer formation relied on small magnitude changes between the size of the observed peaks in size exclusion chromatography, which are possibly the result of the variable levels of disulfide formation observed between different MinD constructs, itself a result of different expression levels. And the purification as a dimer could be the result of a complete conversion to disulfide dimer, which is likely dependent on purification conditions. As these are the only studies previously done on $\mathrm{MinD_{Ng}}$ dimerization, our results are the first to suggest that ATP binding does not give rise to self-association of $\mathrm{MinD_{Ng}}$ in the absence of the membrane.

4.2 $\mathrm{MinD_{Ng}}$ does not form a dimer in the presence of ATP

The dimerization behaviour of $\mathrm{MinD_{Ec}}$ with ATP is well characterized with complete conversion to a dimeric form being observed by size exclusion chromatography (26, 29). However, replicating these results with $\mathrm{MinD_{Ng}}$ has proven impossible, suggesting that $\mathrm{MinD_{Ng}}$ does not form a dimer in solution. In contrast, $\mathrm{MinD_{Ng}}$ is likely to form a dimer on membranes, since its ATP hydrolysis activity is stimulated by MinE, and the MinE binding site on MinD is formed at the dimer interface, spanning both subunits (43). Our His-tagged MinD_{Ng} also displays cooperative stimulation of its ATPase activity by MinE, again suggesting dimerization. This suggests that at some point in the ATPase cycle MinD_{Ng} does form a dimer, even though our experiments were not able to detect this directly. One possible explanation for the absence of MinD_{Ng} dimerization may be potential interference caused by the presence of the hexahistadine tag. However, the mechanism of this interference is unclear, as the C-terminus of MinD lies away from the dimeric interface. We cannot rule out the possibility of an allosteric affect caused by the His-tag that is transmitted through to the dimer interface through an unknown mechanism. In the future it would be useful to do an experiment with a MinD_{Ec}-hexahistadine fusion protein, or by repeating experiments on a MinD_{Ng} protein that does not have a hexahistadine tag.

An alternate hypothesis that is consistent with the lack of MinD dimerization in the absence of membrane is that the timing of dimerization in the Min cycle may be flexible, where MinD_{Ng} dimerization only occurs after membrane binding. It has been shown that after binding ATP the MTS mediates membrane interactions. As ATP hydrolysis is only observed in the presence of membranes, membrane binding must alter the conformation of MinD in a way that is communicated to the active site. As the active site is formed at the dimer interface, it is possible that MinD_{Ng} requires membrane binding before dimer formation, a behaviour seen in a family of related P-loop GTPase proteins (82, 83). While it was beyond the scope of this thesis to test this hypothesis, in the future it may be possible to probe dimerization using alternate techniques that are compatible with lipid binding (e.g. fluorescence resonance energy transfer).

4.3 Prospects for solution NMR of MinD

With the advent of higher magnetic field strengths and cryoprobe technology, it has been possible to use solution NMR to study proteins of increasing sizes. Nonetheless, MinD_{Ng} still suffers from the poor relaxation properties of a large protein system. This made it a challenge to obtain chemical shift assignments, since the 3D triple-resonance experiments needed for chemical shift assignment tended to show poor signal-to-noise. Fortunately, significant gains in sensitivity could be realized by the use of uniform ^{2}H labeling. For example, the HNCA experiment detected less than ¼ the expected correlations without deuteration; with deuteration, the number of observed correlations was more than doubled.

It is interesting to note that very few residues near the active site could be assigned. While there are a small number of unassigned peaks in the ^{1}H – ^{15}N TROSY spectrum that that could account for the 70 unassigned residues, it is clear that there are still a significant number of missing peaks, likely due to severe peak broadening. Broadening can be caused by chemical exchange between two or more states on a timescale that is detrimental for solution NMR (i.e. microsecond to millisecond). Addition of ADP or ATP reduced the quality of spectra further, although this is most likely attributed to reduced sample solubility. Given that these residues are also involved in formation of the dimeric interface, this broadening may reflect conformational flexibility, where the dimeric conformation is in exchange with the monomeric conformation. Another possibility is that the K_D for dimer formation in the absence of lipids is not low enough to observe the dimer by size exclusion chromatography at the concentrations tested (<50uM), while at concentrations used for NMR (~1mM) an appreciable population of dimer may be present. Although this might be expected to yield peaks from both species, the number of peaks suggests that the alternate state, if present, is not present in sufficient quantities to allow its detection. Alternatively, the dimeric state may not be directly detected in these spectra, but may be the source of peak broadening, with on and off-rates being on the millisecond to microsecond timescale that leads to peak broadening. It is also possible that these regions of the protein are intrinsically dynamic, a possibility that is supported by high B-factors in these regions in the crystal structure of ADP-bound MinD (42).

4.4 MinD$_{Ng}$ has equal affinity for ADP and ATP

Another surprising result was the similarity in MinD$_{Ng}$ binding affinity for ATP and ADP, particularly since ATP is required for membrane localization. The functionality of the Min system relies on the ability of MinD to replace bound ADP with ATP, which in a situation of equal affinities, would not favor ATP, particularly since intracellular concentrations of ATP and ADP are very similar in *E. coli*, on the range of 1 mM (84). With an equal affinity, it would be expected that nucleotide exchange would occur in both directions: after binding ATP and the membrane, ATP could be exchanged for ADP, which would be expected to result in breakup of the membrane-bound MinD complex, but this is not observed. This suggests that the affinity for ATP increases, possibly the result of conformational changes due to membrane binding.

While surprising, there is precedent for these K_D measurements. A related P-loop GTPase, MipZ, displays nearly identical affinity for ADP and ATP analogues, although the affinities are 10-fold stronger than seen for MinD (85). When analyzing crystal structures of ADP- and ATP-bound MinD, The number of hydrogen bonds between MinD and ADP or ATP are identical, suggesting that MinD binds ADP as strongly as ATP (42). This is consistent with the experimental data, however this is neglecting possible interactions through Van der Waals forces or electrostatics, which is likely to contribute significantly due to the electron-dense phosphate groups.

Unfortunately, there were no assigned residues that directly participate in nucleotide binding. While nucleotide-dependent changes in chemical shifts were measured to calculate the K_D, it is not clear that the event being measured is due to nucleotide binding. It remains possible the change in chemical shifts observed upon incubation with nucleotides arise from some process occurring after nucleotide binding takes place. Such a process is likely not dimerization as that has not been observed in size exclusion chromatography, but may instead be the result of conformational changes that give rise to membrane binding. However, this conformational change would not be expected to occur with ADP binding. Instead there are subtle differences between the ADP- and ATP-bound spectra which may be the result of these conformational changes required for membrane binding. In this scenario loading of any nucleotide results in conformational changes in MinD, but only ATP results in the change necessary to bind the membrane. Unfortunately it will be difficult to eliminate this possibility in the absence of assigned residues in the ATP binding site.

4.5 MinD nucleotide binding is a slow process

While results from this thesis set the stage for future experiments to directly measure rates of ADP and ATP binding to MinD, some information on these rates can already be gleamed from the spectra of the partially-saturated nucleotide-bound species. In the presence of nucleotide at half-saturating concentrations, two peaks can be seen for several residues. This suggests the rate of exchange is slower than the NMR timescale, being in the millisecond range. An upper limit of exchange rates can be ascertained by application of Equation 1.6 to the chemical shift difference of peaks between the two exchanging species. In order to resolve two independent peaks, two conditions must be met: the rate of exchange must be slower than the NMR timescale, and that the rate of exchange is slower than the coalescence point of the two peaks. In the case of G130, a shift difference of 0.098 ppm can be resolved in the ^{15}N dimension, which corresponds to 6Hz at the spectrometer field strength used. Exchange between the two states must therefore be slower than $6s^{-1}$, which corresponds to a lifetime of 170ms.

Computational models require slow nucleotide exchange rates to facilitate diffusion of MinD between the cell poles once it is liberated from the membrane. Cytoplasmic diffusion rates of MinD have been measured at $16\mu m^2/s$ (86). For a 170ms period, MinD is expected to diffuse $2.7\mu m^2$ before nucleotide exchange (and presumably rapid membrane binding) occurs. An *E. coli* cell can be approximated as 2µm in length and 1µm in width (87). Knowing that average displacement can be approximated by $\tau \cong \frac{x^2}{D}$

(88), it is possible to estimate that MinD can travel an average of 1.6μm before undergoing nucleotide exchange, which is nearly equal to the length of the cell. Indeed for *N. gonorrhoeae*, whose cell morphology is better approximated as a sphere of radius 1μm (89), this would suggest MinD has a very high probability of traveling from one cell pole to another, and potentially even back again. The average residency time for cytoplasmic MinD was determined to be 300ms which is also in good agreement with the exchange rate measured (86). Together, this data strongly suggests that nucleotide exchange is indeed a slow process, and may be ultimately responsible for prevention of rapid rebinding to the membrane, allowing MinD to diffuse between MinD-rich zones.

In the future better characterization of nucleotide binding rates could be achieved by performing a ZZ-exchange experiment. While it is the preferred technique to measure dynamics on the millisecond timescale, the spectral quality of the nucleotide-bound MinD samples may preclude use of this experiment: ZZ-Exchange requires the ability to resolve and integrate weak cross-peaks. Peaks in our spectra are already of low intensity, creating challenges for the accurate measurement of cross-peak volumes. Instead the CPMG experiment may prove useful since it is able to measure rates for slower dynamic processes and may have better sensitivity than the ZZ-exchange method. Ultimately the rates measured in this work can be used in future models of Min protein reaction diffusion models, leading to better understanding of how this relatively simple system can give rise to the long-range dynamic pattern formation that is responsible for regulating cell division site selection in pathogenic bacteria.

4.6 Conclusion

Many models of Min protein oscillation require that nucleotide exchange occur on the millisecond to second timescale While in this thesis the rates of binding were not directly measured, constraints placed on them suggest the assumption of slow nucleotide exchange is valid. Through resonance assignments of backbone atoms I have enabled the precise measurement of these rates by NMR. Future experiments should be performed to measure the rate of binding of both ADP and ATP, and to measure the rate of exchange of bound ADP for ATP. I have shown that MinD_{Ng} does not form an ATP-dependent dimer in contrast with existing models. Instead a disulfide-mediated dimer was observed, which can be used to explain the conflicting reports of dimerization in MinD_{Ng}. Solution NMR was employed to determine affinities for ADP and ATP. The indistinguishable affinities for ADP and ATP suggest that in the cytosol, MinD does not preferentially bind ATP. Instead it likely relies on another interaction to alter its affinity for ATP in order to stabilize the membrane-bound dimeric species, possibly membrane interaction itself. Validation of the dimerization results should also be carried out with a MinD_{Ec}-

hexahistadine fusion protein to rule out interference from the hexahistadine tag. While questions remain, the understanding of conditions necessary for Min protein oscillation *in vivo* will lead to identification of possible modes of inhibition, which are invaluable for the development of new antibiotics.

References

1. Adler HI, Fisher WD, Cohen A, Hardigree AA (1967) Miniature escherichia coli cells deficient in DNA. *Proc Natl Acad Sci* 57(2):321–326.

2. Teather RM, Collins JF, Donachie WD (1974) Quantal Behavior of a Diffusible Factor Which Initiates Septum Formation at Potential Division Sites in Escherichia coli. *J Bacteriol* 118(2):407–413.

3. Davie E, Sydnor K (1984) Genetic Basis of Minicell Formation. *J Bacteriol* 158(3):1202–1203.

4. Pichoff S, Vollrath B, Touriol C, Bouché J-P (1995) Deletion analysis of gene minE which encodes the topological specificity factor of cell division in Escherichia coil. *Mol Microbiol* 18(2):321–329.

5. de Boer PAJ, Crossley RE, Rothfield LI (1989) A division inhibitor and a topological specificity factor coded for by the minicell locus determine proper placement of the division septum in E. coli. *Cell* 56(4):641–649.

6. de Boer PA, Crossley RE, Rothfield LI (2006) Central role for the Escherichia coli minC gene product in two different cell division-inhibition systems. *Proc Natl Acad Sci* 87(3):1129–1133.

7. Hu Z, Mukherjee A, Pichoff S, Lutkenhaus J (1999) The MinC component of the division site selection system in Escherichia coli interacts with FtsZ to prevent polymerization. *Proc Natl Acad Sci* 96(26):14819–14824.

8. Ventola CL (2015) The antibiotic resistance crisis: causes and threats. *P T J* 40(4):277–83.

9. Dillon JAR, et al. (2006) Challenges in the control of gonorrhea in South America and the Caribbean: Monitoring the development of resistance to antibiotics. *Sex Transm Dis* 33(2):87–95.

10. Unemo M, Nicholas RA (2012) Emergence of multidrug-resistant, extensively drug-resistant and untreatable gonorrhea. *Future Microbiol* 7(12):1401–1422.

11. Wi T, et al. (2017) Antimicrobial resistance in Neisseria gonorrhoeae: Global surveillance and a call for international collaborative action. *PLOS Med* 14(7):e1002344.

12. Ramirez-Arcos S, et al. (2001) Deletion of the cell-division inhibitor MinC results in lysis of Neisseria gonorrhoeae. *Microbiology* 147(1):225–237.

13. Parti RP, et al. (2011) Attenuated virulence of min operon mutants of Neisseria gonorrhoeae and

their interactions with human urethral epithelial cells. *Microbes Infect* 13(6):545–554.

14. Parti RP, Horbay MA, Liao M, Dillon J-AR (2013) Regulation of minD by oxyR in Neisseria gonorrhoeae. *Res Microbiol* 164(5):406–415.

15. Lutkenhaus J, Pichoff S, Du S (2014) Bacterial cytokinesis : from Z ring to divisome. *Cytoskeleton* 69(10):778–790.

16. Szeto J, et al. (2001) Gonococcal MinD Affects Cell Division in Neisseria gonorrhoeae and Escherichia coli and Exhibits a Novel Self-Interaction. *J Bacteriol* 183(21):6253–6264.

17. Ramirez-arcos S, Szeto J, Dillon JR, Margolin W (2002) Conservation of dynamic localization among MinD and MinE orthologues : oscillation of Neisseria gonorrhoeae proteins in Escherichia coli. *Mol Microbiol* (2):493–504.

18. Shih Y-L, Le T, Rothfield L (2003) Division site selection in Escherichia coli involves dynamic redistribution of Min proteins within coiled structures that extend between the two cell poles. *Proc Natl Acad Sci* 100(13):7865–7870.

19. Hu Z, Gogol EP, Lutkenhaus J (2002) Dynamic assembly of MinD on phospholipid vesicles regulated by ATP and MinE. *Proc Natl Acad Sci U S A* 99(10):6761–6766.

20. Suefuji K, Valluzzi R, RayChaudhuri D (2002) Dynamic assembly of MinD into filament bundles modulated by ATP, phospholipids, and MinE. *Proc Natl Acad Sci* 99(26):16776–16781.

21. Fu X, Shih Y-L, Zhang Y, Rothfield LI (2001) The MinE ring required for proper placement of the division site is a mobile structure that changes its cellular location during the Escherichia coli division cycle. *Proc Natl Acad Sci* 98(3):980–985.

22. de Boer PA, Raskin DM (1999) Rapid pole-to-pole oscillation of a protein required for directing division to the middle of Escherichia coli. *Proc Natl Acad Sci U S A* 96(9):4971–6.

23. Raskin DM, de Boer PA (1999) MinDE-dependent pole-to-pole oscillation of division inhibitor MinC in Escherichia coli. *J Bacteriol* 181(20):6419–24.

24. Loose M, Fischer-friedrich E, Ries J, Kruse K, Schwille P (2008) Spatial Regulators for Bacterial Cell. *Science* 320(May):789–792.

25. Loose M, Fischer-Friedrich E, Herold C, Kruse K, Schwille P (2011) Min protein patterns emerge

from rapid rebinding and membrane interaction of MinE. *Nat Struct Mol Biol* 18(5):577–583.

26. Zhou H, et al. (2005) Analysis of MinD Mutations Reveals Residues Required for MinE Stimulation of the MinD ATPase and Residues Required for MinC Interaction. *J Bacteriol* 187(2):629–638.

27. Szeto J, Eng NF, Acharya S, Rigden MD, Dillon JAR (2005) A conserved polar region in the cell division site determinant MinD is required for responding to MinE-induced oscillation but not for localization within coiled arrays. *Res Microbiol* 156(1):17–29.

28. Hu Z, Saez C, Lutkenhaus J (2003) Recruitment of MinC, an Inhibitor of Z-Ring Formation, to the Membrane in Escherichia coli: Role of MinD and MinE. *J Bacteriol* 185(1):196–203.

29. Hu Z, Lutkenhaus J (2003) A conserved sequence at the C-terminus of MinD is required for binding to the membrane and targeting MinC to the septum. *Mol Microbiol* 47(2):345–355.

30. Szeto TH, Rowland SL, Habrukowich CL, King GF (2003) The MinD membrane targeting sequence is a transplantable lipid-binding helix. *J Biol Chem* 278(41):40050–40056.

31. Lackner LL, Raskin DM, De Boer PAJ (2003) ATP-dependent interactions between Escherichia coli Min proteins and the phospholipid membrane in vitro. *J Bacteriol* 185(3):735–749.

32. Zhou H, Lutkenhaus J (2005) MinC mutants deficient in MinD- and DicB-mediated cell division inhibition due to loss of interaction with MinD, DicB, or a septal component. *J Bacteriol* 187(8):2846–2857.

33. Huang J, Cao C, Lutkenhaus J (1996) Interaction between FtsZ and inhibitors of cell division. *J Bacteriol* 178(17):5080–5085.

34. Ma L, King GF, Rothfield L (2004) Positioning of the MinE binding site on the MinD surface suggests a plausible mechanism for activation of the Escherichia coli MinD ATPase during division site selection. *Mol Microbiol* 54(1):99–108.

35. Hu Z, Lutkenhaus J (2001) Topological Regulation of Cell Division in E . coli : Spatiotemporal Oscillation of MinD Requires Stimulation of Its ATPase by MinE and Phospholipid. *Mol Cell* 7:1337–1343.

36. Ghasriani H, et al. (2010) Appropriation of the MinD protein-interaction motif by the dimeric interface of the bacterial cell division regulator MinE. *Proc Natl Acad Sci* 107(43):18416–18421.

37. Szeto TH, Rowland SL, Rothfield LI, King GF (2002) Membrane localization of MinD is mediated by a C-terminal motif that is conserved across eubacteria , archaea , and chloroplasts. *Proc Natl Acad Sci* 99(24):15693–15698.

38. Zhou H, Lutkenhaus J (2003) Membrane Binding by MinD Involves Insertion of Hydrophobic Residues within the C-Terminal Amphipathic Helix into the Bilayer. *J Bacteriol* 185(15):4326–4335.

39. Walker JE, Saraste M, Runswick MJ, Gay NJ (1982) Distantly related sequences in the alpha- and beta-subunits of ATP synthase, myosin, kinases and other ATP-requiring enzymes and a common nucleotide binding fold. *EMBO J* 1(8):945–51.

40. James Milner-White E, Coggins JR, Anton IA (1991) Evidence for an ancestral core structure in nucleotide-binding proteins with the type A motif. *J Mol Biol* 221(3):751–754.

41. Leipe DD, Koonin E V., Aravind L (2003) Evolution and classification of P-loop kinases and related proteins. *J Mol Biol* 333(4):781–815.

42. Hayashi I, Oyama T (2001) Structural and functional studies of MinD ATPase : implications for the molecular recognition of the bacterial cell division apparatus. *EMBO J* 20(8):1819–1828.

43. Wu W, Park K-T, Holyoak T, Lutkenhaus J (2011) Determination of the structure of the MinD–ATP complex reveals the orientation of MinD on the membrane and the relative location of the binding sites for MinE and MinC. *Mol Microbiol* 79(6):1515–1528.

44. Cordell SC, Anderson RE, Löwe J (2001) Crystal structure of the bacterial cell division inhibitor MinC. *EMBO J* 20(10):2454–2461.

45. Park KT, Wu W, Lovell S, Lutkenhaus J (2012) Mechanism of the asymmetric activation of the MinD ATPase by MinE. *Mol Microbiol* 85(2):271–281.

46. Ayed SH, et al. (2017) Dissecting the role of conformational change and membrane binding by the bacterial cell division regulator MinE in the stimulation of MinD ATPase activity. *J Biol Chem* 292(50):20732–20743.

47. Howard M, Kruse K (2005) Cellular organization by self-organization: Mechanisms and models for Min protein dynamics. *J Cell Biol* 168(4):533–536.

48. Kruse K, Howard M, Margolin W (2007) An experimentalist's guide to computational modelling of

the Min system. *Mol Microbiol* 63(5):1279–1284.

49. Kondo S, Miura T, Turing T (2010) Reaction-Diffusion Model as a Framework for Understanding Biological Pattern Formation. *Science (80-)* 329(September):1616–1620.

50. Okazawa N, Sorensen TS (1978) The line-shape analysis of nuclear magnetic resonance peaks broadened by the presence of a “hidden” exchange partner. *Can J Chem* 56(21):2737–2742.

51. Farrow NA, Zhang O, Forman-Kay JD, Kay LE (1994) A heteronuclear correlation experiment for simultaneous determination of 15 N longitudinal decay and chemical exchange rates of systems in slow equilibrium. *J Biomol NMR* 4(5):727–734.

52. Tollinger M, Skrynnikov NR, Mulder FAA, Forman-Kay JD, Kay LE (2001) Slow dynamics in folded and unfolded states of an SH3 domain. *J Am Chem Soc* 123(46):11341–11352.

53. Pervushin K, Riek R, Wider G, Wüthrich K (1997) Attenuated T2 relaxation by mutual cancellation of dipole–dipole coupling and chemical shift anisotropy.pdf. *Proc Natl Acad Sci U S A* 94(November):12366–12371.

54. Ikura M, Kay LE, Bax A (1990) A novel approach for sequential assignment of 1H, 13C, and 15N spectra of larger proteins: Heteronuclear triple-resonance three-dimensional NMR spectroscopy. Application to calmodulin. *Biochemistry* 29(19):4659–4667.

55. Grzesiek S, Bax A (1993) Amino acid type determination in the sequential assignment procedure of uniformly 13 C/15 N-enriched proteins. *J Biomol NMR* 3(2):185–204.

56. Grzesiek S, Bax A (1992) Correlating backbone amide and side chain resonances in larger proteins by multiple relayed triple resonance NMR. *J Am Chem Soc* 114(16):6291–6293.

57. Wittekind M, Mueller L (1993) HNCACB, a high-sensitivity 3D NMR experiment to correlate amide-proton and nitrogen resonances with the alpha-and beta-carbon resonances in proteins. *J Magn Reson* 101:201–205.

58. Grzesiek S, Bax A (1992) An efficient experiment for sequential backbone assignment of medium-sized isotopically enriched proteins. *J Magn Reson* 99(1):201–207.

59. Clubb RT, Thanabal V, Wagner G (1992) A constant-time three-dimensional triple-resonance pulse scheme to correlate intraresidue 1HN, 15N, and 13C’chemical shifts in 15N---13C-labelled proteins.

60. Dalgarno DC, Levine BA, Williams RJP (1983) Structural information from NMR secondary chemical shifts of petide alpha C-H protons in proteins. *Biosci Rep* 3:443–452.

61. Tamiola K, Mulder FAA (2012) Using NMR chemical shifts to calculate the propensity for structural order and disorder in proteins. *Biochem Soc Trans* 40(5):1014–1020.

62. Lacabanne D, Meier BH, Böckmann A (2018) Selective labeling and unlabeling strategies in protein solid-state NMR spectroscopy. *J Biomol NMR* 71(3):141–150.

63. Prasanna C, Dubey A, Atreya HS (2015) *Amino Acid Selective Unlabeling in Protein NMR Spectroscopy* (Elsevier Inc.). 1st Ed. doi:10.1016/bs.mie.2015.05.008.

64. Shortle D (1994) Assignment of amino acid type in 1H-15N correlation spectra by labeling with 14N-amino acids. *J Magn Reson B* 105(1):88–90.

65. Krishnarjuna B, Jaipuria G, Thakur A, D'Silva P, Atreya HS (2011) Amino acid selective unlabeling for sequence specific resonance assignments in proteins. *J Biomol NMR* 49(1):39–51.

66. Dubey A, Kadumuri V, Jaipuria G (2016) Rapid NMR Assignments of Proteins by Using Optimized Combinatorial Selective Unlabeling. *ChemBioChem* 17:334–340.

67. Bellstedt P, et al. (2013) Resonance assignment for a particularly challenging protein based on systematic unlabeling of amino acids to complement incomplete NMR data sets. *J Biomol NMR* 57:65–72.

68. Ausubel FM, et al. (2003) *Current Protocols in Molecular Biology Current Protocols in Molecular Biology* (John Wiley & Sons).

69. Eng NF, Szeto J, Acharya S, Tessier D, Dillon JR (2006) The C-terminus of MinE from Neisseria gonorrhoeae acts as a topological specificity factor by modulating MinD activity in bacterial cell division. *Res Microbiol* 157:333–344.

70. Smith PK, et al. (1985) Measurement of protein using bicinchoninic acid. *Anal Biochem* 150(1):76–85.

71. Schägger H (2006) Tricine-SDS-PAGE. *Nat Protoc* 1(1):16.

72. MacDonald RC, et al. (1991) Small-volume extrusion apparatus for preparation of large, unilamellar vesicles. *BBA - Biomembr* 1061(2):297–303.

73. Rueden CT, et al. (2017) ImageJ2: ImageJ for the next generation of scientific image data. *BMC Bioinformatics* 18(1):529.

74. Wojdyr M (2010) Fityk : a general-purpose peak fitting program. *J Appl Crystallogr* 43(5):1126–1128.

75. Delaglio F, et al. (1995) NMRPipe: a multidimensional spectral processing system based on UNIX pipes. *J Biomol NMR* 6(3):277–293.

76. Johnson BA, Blevins RA (1994) NMR View: A computer program for the visualization and analysis of NMR data. *J Biomol NMR* 4(5):603–614.

77. Venters RA, et al. (1995) High-level 2H/13C/15N labeling of proteins for NMR studies. *J Biomol NMR* 5(4):339–344.

78. Atreya HS, Chary KVR (2000) Amino acid selective “unlabelling” for residue-specific NMR assignments in proteins. *Curr Sci* 79(4):504–507.

79. Waterhouse A, et al. (2018) SWISS-MODEL: homology modelling of protein structures and complexes. *Nucleic Acids Res* 46(W1):W296--W303.

80. Benkert P, Biasini M, Schwede T (2010) Toward the estimation of the absolute quality of individual protein structure models. *Bioinformatics* 27(3):343–350.

81. de Boer PA, Crossley RE, Hand AR, Rothfield LI (1991) The MinD protein is a membrane ATPase required for the correct placement of the Escherichia coli division site. *EMBO J* 10(13):4371–80.

82. Lutkenhaus J (2012) The ParA/MinD family puts things in their place. *Trends Microbiol* 20(9):411–418.

83. Lin W-C, et al. (2014) H-Ras forms dimers on membrane surfaces via a protein-protein interface. *Proc Natl Acad Sci* 111(8):2996–3001.

84. Albe KR, Butler MH, Wright BE (1990) Cellular concentrations of enzymes and their substrates. *J Theor Biol* 143(2):163–195.

85. Kiekebusch D, Michie KA, Essen L-O, Löwe J, Thanbichler M (2012) Localized dimerization and nucleoid binding drive gradient formation by the bacterial cell division inhibitor MipZ. *Mol Cell* 46(3):245–59.

86. Meacci G, et al. (2006) Mobility of Min-proteins in Escherichia coli measured by fluorescence correlation spectroscopy. *Phys Biol* 3(4):255–263.

87. Zaritsky A, Woldringh CL (1978) Chromosome replication rate and cell shape in Escherichia coli: Lack of coupling. *J Bacteriol* 135(2):581–587.

88. Milo R, Phillips R (2015) *Cell biology by the numbers* (Garland Science).

89. Westling Haggstrom B, Elmros T, Normark S, Winblad B (1977) Growth pattern and cell division in Neisseria gonorrhoeae. *J Bacteriol* 129(1):333–342.

90. Bateman A (2019) UniProt: A worldwide hub of protein knowledge. *Nucleic Acids Res* 47(D1):D506–D515.

91. Madeira F, et al. (2019) The EMBL-EBI search and sequence analysis tools APIs in 2019. *Nucleic Acids Res*. doi:10.1093/nar/gkz268.

92. Henikoff S, Henikoff JG (1992) Amino acid substitution matrices from protein blocks. *Proc Natl Acad Sci U S A* 89(22):10915–9.

93. Waterhouse AM, Procter JB, Martin DMA, Clamp M, Barton GJ (2009) Jalview Version 2-A multiple sequence alignment editor and analysis workbench. *Bioinformatics* 25(9):1189–1191.